



HAL
open science

Lowland gravel-bed river recovery through former mining reaches, the key role of sand

Thomas Dépret, Clément Virmoux, Emmanuèle Gautier, Hervé Piégay, Mariya Doncheva, Brian Plaisant, Sirine Ghamgui, Evan Mesmin, Ségolène Saulnier-Copard, Lucile de Milleville, et al.

► To cite this version:

Thomas Dépret, Clément Virmoux, Emmanuèle Gautier, Hervé Piégay, Mariya Doncheva, et al.. Lowland gravel-bed river recovery through former mining reaches, the key role of sand. *Geomorphology*, 2021, 373, pp.107493. 10.1016/j.geomorph.2020.107493 . hal-03793233

HAL Id: hal-03793233

<https://hal.science/hal-03793233>

Submitted on 21 Nov 2022

HAL is a multi-disciplinary open access archive for the deposit and dissemination of scientific research documents, whether they are published or not. The documents may come from teaching and research institutions in France or abroad, or from public or private research centers.

L'archive ouverte pluridisciplinaire **HAL**, est destinée au dépôt et à la diffusion de documents scientifiques de niveau recherche, publiés ou non, émanant des établissements d'enseignement et de recherche français ou étrangers, des laboratoires publics ou privés.



Distributed under a Creative Commons Attribution - NonCommercial 4.0 International License

1 **Lowland gravel-bed river recovery through former mining reaches, the key role of sand**

2

3 Thomas Dépret ^a, Clément Virmoux ^a, Emmanuèle Gautier ^b, Hervé Piégay ^c, Mariya Doncheva ^b,
4 Brian Plaisant ^b, Sirine Ghamgui ^b, Evan Mesmin ^b, Ségolène Saulnier-Copard ^a, Lucile de Milleville ^d,
5 Julien Caverro ^a, Pablo Hamadouche ^b

6

7 ^a Laboratoire de Géographie Physique, CNRS UMR8591, 1 Place Aristide Briand, 92195 Meudon,
8 France

9 ^b Université Paris 1 Panthéon-Sorbonne, Laboratoire de Géographie Physique, CNRS UMR8591, 1
10 Place Aristide Briand, 92195 Meudon, France

11 ^c Université de Lyon, CNRS, UMR 5600 - Environnement-Ville-Société, Site ENS de Lyon, 15 Parvis
12 René Descartes, Lyon 69342, France

13 ^d Université de Paris Est-Créteil, Laboratoire de Géographie Physique, CNRS UMR8591, 1 Place
14 Aristide Briand, 92195 Meudon, France

15

16

17 **Abstract**

18 Whereas the geomorphic effects of in-channel mining have been widely documented, very few studies
19 have focused on recovery trajectories after mining ended. This paper describes and quantifies the
20 channel adjustment of extended and over-widened mining pits located in a low energy gravel-bed
21 river, and identifies the factors that control their recovery rate. The study was based on aerial
22 photographs and LiDAR analysis, grain-size sampling, bedload computation and geophysical
23 measurements made during ground penetrating radar (GPR) and electrical resistivity tomography
24 (ERT) surveys. We describe the spatio-temporal changes in the morphology of former pits as well as
25 the current surficial longitudinal grain-size pattern in pits and in neighbouring upstream and
26 downstream reaches. Our results show a wide range of geomorphic readjustments. Between 23 and 47
27 yr after the end of mining, the mining reaches have still not yet fully recovered. The planimetric
28 recovery rate is closely correlated with the ratio of the volume deposited in the pits to their original

29 volume. Finally, the infilled material is only partly composed of bedload and the mainly sandy fine
30 sediments play a primary role in the recovery process. The abundance of sand, controlled by the
31 lithology of the watershed, explains the unexpectedly high recovery rates of some pits despite the low
32 energy of the river.

33

34

35 **Keywords**

36 Channel mining; Geomorphic resilience; Sand; Low-energy river

37

38

39 **Highlights**

- 40 - Characterisation of morphological and grain-size recovery of former in-channel pits
- 41 - Adjustment still underway 27-47 years after mining stopped
- 42 - Recovery rate controlled by pit volume, the volume of sediment supplied and pit trap
43 efficiency
- 44 - The sand load plays an essential role in recovery processes
- 45 - Catchment lithology also crucial in recovery

46

47

48 **1. Introduction**

49 The alluvial resources provided by river corridors have been overused worldwide since the end of
50 World War II because of the advent of concrete as a building material and to growing development.
51 The detrimental social and environmental effects of this mining has led to control of, or to a complete
52 ban on gravel mining in many countries in recent decades (Kondolf, 1997; Rinaldi et al., 2005). Gravel
53 mining directly or indirectly modifies both the river bed geometry and the substrate, can lead to a
54 profound and long-lasting alteration of aquatic and riparian habitats as well as to the destruction or
55 weakening of fluvial engineering structures and loss of alluvial groundwater storage thereby reducing
56 water resources (Kondolf, 1994; Bravard et al., 1997; Bravard et al., 1999a; Brown et al., 1998;

57 Koehnken et al., 2020). Although these effects and the factors that control them are widely
58 documented (e.g., Bull and Scott, 1974; Collins and Dunne, 1989; Kondolf, 1994, 1997; Surian and
59 Rinaldi, 2003; Simon and Rinaldi, 2006; Wyzga, 2007; Sreebha and Padmalal, 2011; Arróspide et al.,
60 2018), very little is known about channel recovery after mining ends.

61 The present review focuses on in-stream dry-pit and wet-pit mining, which, as defined by Kondolf,
62 (1994), both consist of dredging a pit in the channel of varying depth, width and length. We excluded
63 bar skimming mining operations (Kondolf, 1994; Rempel and Church, 2009), defined as the scalping
64 of the dry surficial layer of bars at low-flow. For these specific cases, both modelling and field
65 approaches have already been explored. Physical, numerical or analytical modelling has focused on
66 the spatio-temporal pattern of pit filling and/or how mining modifies hydrodynamics and bed
67 morphology (e.g., Fredsoe, 1979; van Rijn, 1986; Kornis and Laczay, 1988; Lee et al., 1993; Gill,
68 1994; Barman et al., 2017, 2018, 2019; Neyshabouri et al., 2002; Cao and Pender, 2004; Chen et al.,
69 2010). These authors particularly highlight the downstream migration of pits as they fill up as well as
70 the degradation of the bed both upstream and downstream from the initial location of the pits. Most
71 studies using these approaches used pit dimensions (pit width \leq channel width, pit length $\leq 2 \times$
72 channel width) that are considerably smaller than those of the pits reported in most rivers (e.g., Lee et
73 al., 1993; Gill, 1994; Barman et al., 2017, 2018, 2019; Neyshabouri et al., 2002; Chen et al., 2010).
74 Two main infill stages have been identified (Lee et al., 1993). During the first stage, termed the
75 convective stage, the maximum scour depth remains relatively constant and the upstream boundary of
76 the pit migrates up to the original downstream edge. The following diffusion stage corresponds to
77 complete pit infill and is characterised by the downstream migration and the progressive reduction of
78 the maximum scour depth. The infilling rate of pits is theoretically controlled by the amount of
79 upstream sediment supplied and by pit trap efficiency (van Rijn, 1986), which in turn, is mainly
80 controlled by pit geometry (Neyshabouri et al., 2002).

81 Field studies have also been conducted to understand pit infilling. Yuill et al. (2016) used time-
82 series bathymetric surveys of a 1.6 km length borrow-pit whose width occupies around a quarter of the
83 lower Mississippi width combined with a 3D morphodynamic model to describe the morphological
84 changes in the pit and to quantify its infilling rate. These authors showed that the pit traps a very small

85 fraction (5-11%) of the sandy bedload passing through it and that the infilling rate depends mainly on
86 the supply of sediment and the dimensions of the pit. Lastly, the pit is hypothesised to be infilled after
87 a period of 4.4 to 10 yr. Using a section of the gravel-bed Semois River (bankfull width = 50-55 m)
88 dredged to a depth of two metres over a distance of one kilometre to prevent downstream flooding,
89 and repeated topographical surveys, Gob et al. (2005) estimated the time needed to return to the initial
90 state of the riverbed at ten years. Trap efficiency was assumed to be total. Many Italian rivers have
91 undergone similar evolutionary trajectories characterised by incision and bed narrowing throughout
92 the second half of the twentieth century because of the combination of human pressure, e.g.,
93 channelling and damming, and gravel extraction (e.g., Surian et al., 2009; Comiti et al., 2011; Scorpio
94 et al., 2015; Scorpio and Roszkopf, 2016; Belletti et al., 2016). These authors investigated recovery
95 processes at the reach scale, mainly highlighting bed aggradation and widening, 15-20 yr after mining
96 ended. The magnitude of recovery was considerably less than the magnitude of the changes caused by
97 mining and is mainly controlled by the degree of coarse sediment connectivity between hillslopes or
98 floodplain and the riverbed. In the Middle Loire River (France), bed incision caused by gravel mining
99 stopped within 15 to 20 yr following the end of mining, but aggradation was only observed in a few
100 short reaches (Latapie et al., 2014). Morpho-sedimentary recovery has also been characterised in
101 ephemeral Mediterranean systems 12 to 24 yr after mining ended (Rovira et al., 2005; Calle et al.,
102 2017; Sanchis-Ibor et al., 2017). Using a sediment budget along an 11-km long reach of the fine
103 gravel-bed Tordera River with a mean incision of 1.5 m, Rovira et al. (2005) determined that the pre-
104 extraction bed level would not be recovered for around 420 yr, and that most aggradation only
105 occurred during small floods in dry periods. Calle et al. (2017) reconstituted the evolution of morpho-
106 sedimentary units of the Rambla de la Viuda from aerial photographs before, during and after gravel
107 mining ended. Using LiDAR analysis and RTK-DGPS surveys, these authors identified a 3.5-m
108 incision that continued to exist 12 yr after a major reduction in mining activity. They pinpointed the
109 role of major floods in the recovery processes but considered the bed degradation to be irreversible at
110 multi-decadal scale because of the lack of in-channel sediment connectivity. Sanchis-Ibor et al. (2017)
111 quantified bed degradation in the Palancia River using LiDAR and aerial photographs and examined
112 its recovery through a morphological recovery index computed by combining the width of the flow

113 and active channels, the total sinuosity index and the channel count index from aerial photographs at
114 each date.

115 In most rivers affected by mining, geomorphic recovery is usually reduced because of fairly low
116 delivery of coarse sediments (e.g., Surian et al., 2009; Comiti et al., 2011; Belletti et al., 2016).
117 Originating from the upstream part of the watershed or from the alluvial stock through lateral erosion,
118 today most of these sediment sources are no longer available because of cumulative basin- and reach-
119 scale effects of human activities (Downs and Piégay, 2019), particularly dams, which trap bedload
120 sediments, and bank protection works (e.g., Nilsson, 2005; Lehner et al., 2011; Graf, 2006; Bravard et
121 al., 1999b; Ollero, 2010; David et al., 2016; Dépret et al., 2017). In low-energy gravel-bed rivers, the
122 potential for readjustment seems to be even lower because of the slowness of the processes. Broadly,
123 even if these rivers are relatively common systems, knowledge of their morphodynamics remains
124 scarce (Dépret et al., 2015, 2017; Lespez et al. 2015) and explains why management practices and
125 restoration actions are often inappropriate (Lespez et al. 2015). In the case of the low-energy gravel-
126 bed River Cher, the focus of this paper, sediments continued to be extracted from the riverbed until the
127 early 1990s (Dépret et al., 2015, 2017) when this kind of mining was banned in France (Malavoi et al.,
128 2011). At several locations along the river course, sediment mining occurred both in the riverbed and
129 the alluvial plain. As a result, the river exhibits pit sections whose length and width are respectively
130 more than ten and two times the width of the ‘natural’ active channel. These sections very likely act in
131 the same way as floodplain pits captured by rivers, temporarily trapping all or most of the bedload
132 (Mossa and Marks, 2011). Because of the analogy with the captured floodplain pits, we termed the
133 over-widened sections of the Cher River pseudo-captures (PCs). PCs may also trap only part of the
134 suspended load. Thanks to these features, PCs are interesting observatories to characterise and
135 understand the mechanisms and potential for geomorphic recovery processes in low-energy gravel-bed
136 rivers. More than 20 yr after the end of mining of the Cher River, recent aerial photographs show
137 varying degrees of PC readjustment, some of which are surprisingly advanced. Following this
138 observation, the aim of this paper is to explain the wide range of adjustment rates by analysing the
139 pseudo-capture geomorphic recovery and by identifying the factors that control the recovery rate. In
140 theory, the recovery rate is mainly controlled by the original volume of the PC, the volume of

141 sediment originating from upstream and the trap efficiency of the PC. The smaller the original volume,
142 the bigger the supply of sediment, especially the bedload volume, and finally, the more sediment
143 trapped in the PC, and the faster the recovery rate. To test this hypothesis, we used an original
144 interdisciplinary methodological approach combining time-series aerial photographs and LiDAR
145 analysis, grain-size sampling, bedload computation and geophysical measurements made using ground
146 penetrating radar (GPR) and electrical resistivity tomography (ERT) surveys. Underground
147 investigations using the two geophysical methods allowed us to confirm some of the results of our
148 analysis of surface data. Finally, we discuss (i) the importance of the suspended load and of the
149 bedload in the recovery processes, (ii) the key role of sand in the recovery processes of low-energy
150 rivers, (iii) the need to consider lithology when estimating recovery potential, and (iv) the relative
151 importance of PCs in the diversity of aquatic and riparian habitats.

152

153

154 **2. Study sites**

155 *Geological and hydrological context*

156 After leaving its source at 713 m asl., the Cher River mainly flows through gorges across steep slopes
157 or in deep valleys with a very narrow floodplain (upstream Cher in Figure 1). The upstream section of
158 the river is located at the northwest end of the low altitude mountainous Massif Central, which mainly
159 consists of crystalline and metamorphic rocks (Larue, 1981, 2011). After 63 km, the Cher alluvial
160 plain begins (Alluvial Cher in Figure 1) and the river becomes single thread with numerous
161 meandering reaches. After first occupying the Tertiary graben of Montluçon, which continues for 45
162 km to the confluence with the Aumance River (Larue, 1981, 2011; Simon-Coinçon et al., 2000), the
163 river then crosses the sedimentary domain of the Parisian Basin, where it joins the Loire River at a 38
164 m asl. Here, the annual average discharge is $90 \text{ m}^3 \text{ s}^{-1}$ and the catchment area covers 13,615 km². The
165 study section is the first 140 km of the Alluvial Cher between Montluçon and Vierzon. Here, the Cher
166 River has developed a meandering pattern for the last millennia (Vayssière et al., 2020). In addition to
167 intense gravel mining in the riverbed from 1950 to 1990, the river is densely equipped with ancient
168 fluvial engineering works including bank protections and weirs that are major obstacles to local

169 sediment supply through lateral erosion (Dépret et al., 2015, 2017; Vayssière et al., 2020). The
170 hydrological regime is mainly influenced by a pluvio-evaporal oceanic climate and is characteristic of
171 lowland rivers in the western part of mid-latitude regions. Maximum flow occurs in February and
172 minimum flow in August. Because of the construction of the Rochebut dam in the early twentieth
173 century, the hydrological regime has become partly artificial, particularly during low flow and
174 especially upstream from the confluence with the Aumance River (Figure 1).

175

176

177 *Gravel mining*

178 The period of gravel mining was reconstituted by examining all aerial photographs taken between
179 1950 and 2016 (available on <https://remonterletemps.ign.fr>) and the archives of the former Directorate
180 for Industry, Research and the Environment (*Direction de l'Industrie, de la Recherche et de*
181 *l'Environnement*, French acronym DRIRE), local state agencies in the Cher and Allier administrative
182 departments. On the aerial photographs, we looked at signs of mining activity indicated by the
183 presence/absence of the equipment and infrastructure required for mining and sediment sorting. In the
184 archives, we found some of the official authorisation documents granted to the mining companies
185 (Rollet et al., 2008). Gravel mining began and expanded between the late 1940s and the early 1970s
186 and ended between 1983 and 1993, except at one study site (PRE) where it ended in 1968 (Table 1).

187

188 *Site selection*

189 Twelve PCs were identified along the 140-km stretch of the river between Montluçon and Vierzon,
190 in aerial photographs taken between 1950 and 2016 (available on <https://remonterletemps.ign.fr>).
191 Among these, we selected six (Figure 1) by excluding those located immediately upstream or
192 downstream from a weir, or complex planform configuration caused by a neighbouring floodplain pit
193 capture after mining. The sites are named using the three first letters of the main municipality in which
194 they are located, from upstream to downstream: AUD, BOU, BRU, SFL, STH and PRE (Figure 1).
195 Their planimetric, hydraulic and grain-size features are summarised in Table 1. Details on the method
196 used to identify these features are given in Section 3.

197

198 **Figure 1** – Location of the study sites.

199

200 **Table 1** – Hydraulic and geometric parameters, grain-size, and periods of gravel mining activity in the
 201 study reaches.

Site	A (km ²)	L PC t ₀ (m)	w PC t ₀ (m)	w up t ₀ (m)	w PC t ₀ / w up t ₀	Ws up (W m ⁻²)	Ws PC t ₀ (W m ⁻²)	D ₅₀ up (mm)	D ₈₄ up (mm)	Start year	End year
AUD	2112	807	131	49	2.7	7-16	4-6	18-44	39-67	1973	1983
BOU	3492	1107	145	48	3	8-15	2-4	8-21	18-41	1950/59- 1967	1983
BRU	3924	1641	106	58	1.8	5-9	1-2	5-24	19-38	1950- 1959	1989
SFL	4298	2079	77	45	1.7	32-52	2-3	11	24	pre-1950	1993
STH	4385	876	96	43	2.2	28-58	3-6	23	59	1950- 1959	1986
PRE	4422	665	183	50	3.4	3-7	1-2	NA	NA	pre-1950	1968

202 A: Watershed area. L PC t₀: Initial length of PCs, with t₀ the ending of gravel mining activity. w PC t₀:

203 Initial width of PCs. w up t₀: Initial width of active bed upstream of PCs. w PC t₀ / w up t₀: ratio

204 between w PC t₀ and w up t₀. Ws up: Range of specific stream power upstream of PCs for discharge

205 not exceeding 0.99 % of time (94.5 m³ s⁻¹ for AUD, 191 m³ s⁻¹ for the other sites) and along reaches

206 whose length is between 12 and 60 times the active bed width (see Section 3 for explanations and the

207 formula). This discharge was chosen to enable comparison of AUD and the other sites, whose

208 hydrological regime differs because of the Aumance River confluence (Figure 1). It is higher than the

209 critical discharge for bedload incipient motion (Dépret et al., 2015, 2017) and close to the bankfull

210 discharge (85 m³ s⁻¹ for AUD, 178-245 m³ s⁻¹ for the other sites) (Dépret, 2014). The specific stream

211 power is given by the following formula: $\rho_w g Q S / w$, where ρ_w is the density of water (1000 kg m⁻³),

212 g is the gravitational acceleration (9.81 m s⁻²), Q is the discharge (m³ s⁻¹), S is the bed slope (m m⁻¹),

213 and w is the bankfull bed width (m). Ws PC t₀: Minimum and mean specific stream power in PC

214 discharge not exceeding 0.99% of time. D₅₀ up and D₈₄ up: Range of size of bed surface material for

215 which respectively 50% and 84% of the number of sediment clasts are smaller (see Section 3 for
216 explanations).

217

218 Between AUD and the five downstream PCs, the discharge is almost doubled because of inputs of
219 water from the Aumance River, the main tributaries of the Cher River between Montluçon and
220 Vierzon (Figure 1). Only minor tributaries join the Cher River between the reference gauge stations
221 and the PCs (Montluçon for AUD and Saint-Amand-Montrond for the other PCs).

222 In AUD, the bedrock is composed of Eocene-Miocene sand and clays and of conglomeratic or non-
223 conglomeratic Stephanian facies, (Turland et al., 1989a, 1989b). In BOU, the bedrock is Triassic
224 sandstone, sands, argillite and dolomite (Lablanche, 1994; Lablanche et al., 1994). In BRU, the
225 bedrock is Middle Jurassic oolitic and bioclastic limestone as well as of Early Jurassic bioclastic
226 limestone, marl and marl-limestone and Eocene lacustrine limestone and clay (Lablanche, 1994;
227 Lablanche et al., 1994). In SFL, the bedrock is Late Jurassic oolitic or stratified limestone (Debrand-
228 Passard et al., 1997a, 1977b). In STH, the bedrock is stratified or unstratified Late Jurassic limestone
229 and Eocene limestone and clay (Debrand-Passard et al., 1997a, 1977b). Finally, the bedrock in PRE is
230 Eocene limestone and clay (Debrand-Passard et al., 1997a, 1977b).

231

232

233 **3. Material and Methods**

234 Our methodological approach combined time-series aerial photographs and LiDAR analysis, grain-
235 size sampling, bedload computation and geophysical measurements using ground penetrating radar
236 (GPR) and electrical resistivity tomography (ERT) surveys.

237

238 **3.1 PC adjustment patterns and recovery rates**

239 The magnitude of PC recovery was determined from planimetric, topographic and granulometric
240 indexes, presented in that order.

241

242 *Planimetric adjustments*

243 Planimetric adjustment of the PCs was characterised from the end of mining to 2016 by digitising
244 the surface colonised by perennial vegetation on all the available aerial photos with a GIS (ArcGIS
245 10.6 - ESRI) (Table 2). Vegetated surfaces were used to characterise planimetric recovery because
246 they are the direct result of infilling of PCs and because they make it possible to precisely describe and
247 quantify the spatial and temporal pattern of floodplain and channel reconstruction. Vegetated surfaces
248 were digitised at a scale ranging from 1:500 to 1:800, allowing a good trade-off between their visual
249 identification and the precise delimitation of their boundaries. Most of the photos from the French
250 National Geographic Institute (*Institut Géographique National, IGN*) or the Centre-Val-de-Loire
251 Regional Direction for the Environment, Planning and Housing (*Direction Régionale de*
252 *l'Environnement, du de l'Aménagement et du Logement, DREAL*) used here were taken at low flow
253 (Table 2). The most recent ones (i.e., most of those taken between 2002 and 2016) were already
254 orthorectified (resolution range: 0.2-1 m). We rectified and georeferenced the others (maximum
255 RMSE among PCs between 1.4 m and 3.2 m; resolution range: 0.25-1.7 m). In addition, we digitised
256 the active channel (formed by flow channels and bare gravel bars) along a 4-km stretch upstream from
257 the entrance of the PCs. From these data, two main metrics were used to describe the magnitude and
258 the recovery rate. The first, named the width index, is the ratio between the mean width of the active
259 channel in and upstream from the PCs. It was computed at t_0 and in 2016. The upstream width is
260 considered here as the reference width. The closer the index is to 1, the more advanced the recovery.
261 Widths were computed using the Fluvial Corridor Toolbox (Roux et al., 2015). The widths correspond
262 to the mean length of cross sections roughly spaced at one active channel width (30 m for AUD, 40-50
263 m for the other PCs). The second metric describes the planimetric recovery rate. It corresponds to the
264 percentage reduction in the initial surface area of the PC. It was obtained through the yearly ratio
265 (expressed in percentage per year) between the surface area colonised by perennial vegetation in 2016
266 and the surface area of the PC at t_0 .

267 In addition, the longitudinal recovery pattern was characterised by computing the width colonised
268 by perennial vegetation (terrestrialised width) at 10-m intervals along the length of the channel and at
269 each date. This procedure enabled us to reconstruct and quantify the spatio-temporal pattern of PC
270 filling.

271

272 **Table 2** – Temporal resolution at which the PCs’ planimetric trajectories were reconstructed. Q =
 273 Discharge. Gauging stations: MTL = Montluçon; STA = Saint-Amand-Montrond.

Site	t_0	First photo	Most recent photo	Study duration (yr)	N° of dates	Photo interval (yr)	Q range ($\text{m}^3 \text{s}^{-1}$)	Min monthly Q ($\text{m}^3 \text{s}^{-1}$)	Gauging station
AUD	1983	1983		33	9	3.7	1.3-6.9	3	MTL
BOU	1983	1983		33	12	2.8	1.9-54.6	7.1	STA
BRU	1989	1994	2016	27	10	2.7	1.9-54.6	7.1	STA
SFL	1993	1994		23	11	2.1	1.9-25.3	7.1	STA
STH	1986	1986		30	12	2.5	1.9-15.1	7.1	STA
PRE	1969	1969		47	18	2.6	1.8-85.5	7.1	STA

274

275

276 *Vertical adjustments*

277 We computed the mean height of the emerged bare and vegetated surfaces above the low-water
 278 level in 2011 from a LiDAR DEM (provided by the DREAL Centre-Val-de-Loire and used ‘as is’)
 279 whose mean vertical precision of the original point cloud was +/- 0.089 m (minimum: +/- 0.15 m). We
 280 also extracted the low-water elevation from the LiDAR DEM (Biron et al., 2013). In the same way as
 281 for the planimetric adjustment, we examined the longitudinal pattern of the height of the emerged
 282 deposits in PCs by computing the mean height along cross sections spaced at 10-m intervals along the
 283 whole length of the channel. Here, we propose two hypotheses. First, a decrease in height in the
 284 downstream direction, expressing the progradation of the deposits through the PCs. Second, the higher
 285 the recovery, and hence the planimetric rate, the smaller the height downstream.

286 For the purpose of comparison, in the same way, we computed the mean height of the ‘old’
 287 floodplain, namely, that of the deposits beyond the limits of the PC and prior to t_0 . This height was
 288 determined on a narrow (30-m wide) strip along the PCs. A 10-m buffer zone was established between
 289 the edge of the PCs and the edge of the 30 m strip to exclude low bank heights from the computation.

290

291

292 *Grain-size adjustments*

293 Lastly, the recovery of PCs was characterised by grain size. We determined the grain size in the PC
294 bed as well as upstream and downstream (at distances ranging between 2.5 km and 4 km). Sediment
295 size was first determined from photos of coarse grain-size patches on each bar along the study reaches.
296 The photos were taken vertically during the 2018 low-flow period and the target area was protected
297 from direct solar radiation. The resolution of the photos was high enough to enable us to identify
298 particles as small as coarse sand. On each photo, we used GIS (ArcGIS 10.6) to measure the apparent
299 b-axis of 100 particles located at the intersection of a regular grid with spacing higher than the
300 maximum longest particle axis (a-axis). Second, sediment size was determined through 400-particle
301 Wolman samples taken on each riffle (the particles were measured with a calliper). Particles were
302 sampled according to a regular grid covering the whole surface of the riffles.

303 We examined the longitudinal pattern of the D_{50} and the D_{95} . Here we hypothesise that grain-size
304 sorting will continue until recovery is complete, the more advanced the recovery, the smaller the
305 decrease in grain size expected downstream.

306

307 **3.2 Size and origin of deposited sediments**

308 We first estimated to what extent suspended load and bedload could have been trapped by PCs at t_0 .
309 For this purpose, we computed their trap efficiency at intervals of $10 \text{ m}^3 \text{ s}^{-1}$ over the whole discharge
310 range throughout the study period and for each grain-size phi interval from fine silt (4-8 μm) to coarse
311 gravel (32-64 mm). We used a simple theoretical reservoir trap efficiency formula developed from
312 modified overflow rate models and for turbulent flows and varying discharge conditions. Originally
313 proposed by the U.S. Environmental Protection Agency (1986, cited in Haan et al., 1994), it was
314 subsequently modified by Verstraeten and Poesen (2000). We applied the formula to PCs because at
315 least during the initial years after mining ended, they may be considered as weir reservoirs. The
316 formula provides an insight into the trap efficiency of the PC at t_0 , with a decrease in efficiency over
317 time as the PC fills up.

318

319
$$TE = 100 \left[\frac{AV_s}{1.2q_p} \right]$$

320 where TE is the trap efficiency (in %), A is the original surface area of the PC (m^2), V_s is the $10^\circ C$
321 clear water settling velocity of each grain size ($m\ s^{-1}$), extracted from Table 5.4 in Julien (2010).

322

323 We then investigated the role of the suspended load and the bedload in the recovery process by
324 estimating the proportion of fine and coarse material (1 mm threshold) in the infilled volumes of BOU.
325 For this purpose, we combined electrical resistivity tomography (ERT) surveys and grain-size
326 sampling (Figure 2). We first conducted 20 ERT surveys and then took 15 samples at different
327 resistivity measuring points (for resistivity values ranging from $82\ \Omega\ m$ to $3535\ \Omega\ m$). ERT profiles
328 were carried out using a Wenner-Schlumberger array (Loke, 2000) that has a strong signal to noise
329 ratio, which means that with the electrode spaced 1 m apart, we can reach an investigation depth of 12
330 m, which is sufficient to map the entire thickness of the infilling of the PCs and the surface of the
331 bedrock. The device we used was a multi-electrode Abem Terrameter LS with 64 electrodes. Field
332 data were acquired in February 2019 and the water table level remained steady throughout the survey
333 period. Data inversion was carried out by Res2dinv software (Loke and Barker, 1996) using a least
334 square inversion technique. All ERT profiles had an RMS error $<5\%$ before five iterations. Eleven of
335 the samples were taken manually at depths ranging from 0.25 to 0.8 m, with the mass of the largest
336 particle being less than 1% of the total mass of the sample, as recommended by Church et al. (1987) to
337 obtain a representative grain size. The four last samples were extracted from a 4-m core drilled in 2019
338 with a Cobra type TT power core drill. These different grain sizes enabled us to establish a
339 relationship between resistivity value and the percentage of sediment volume of less than 1 mm. We
340 then applied this relationship to each of the resistivity measuring points to estimate the percentage of
341 sediment volume less than 1 mm in the vicinity of these points. Bedrock elevation was obtained
342 through complementary GPR surveys and was validated thanks to the existence of logs from locations
343 close to the PCs (see Section 3.3).

344

345 **Figure 2** – Location of electrical resistivity surveys and grain-size samples in BOU PC.

346

347 To estimate the contribution of bedload to the recovery process, we compared the volumes
348 deposited in the PCs (see Section 3.3) with a maximum estimation of the bedload volumes from
349 Recking's formula (2010, 2013). Four calculation steps are needed to get these estimations:

350 (1) Calculation of the critical Shields number for the D_{84} surface:

351
$$\tau_{c84}^* = (5S + 0.06) \left(\frac{D_{84}}{D_{50}} \right)^{4.4\sqrt{S}-1.5}$$

352 where S is the bed slope (m m^{-1}), D_{50} is the median (m) and D_{84} is the 84th percentile of the bed
353 surface grain-size distribution (m).

354

355 (2) Calculation of the Shields number applied to the D_{84} for a given discharge:

356
$$\tau_{84}^* = \frac{S}{(s-1)D_{84} \left[2/w + 74p^{2.6}(gS)^p q^{-2p} D_{84}^{3p-1} \right]}$$

357 where S is the bed slope (m m^{-1}), w is the bankfull width (m), g is gravitational acceleration (9.81 m s^{-2}),
358 q is the specific discharge ($\text{m}^3 \text{ s}^{-1} \text{ m}^{-1}$) defined by the ratio of flow discharge to channel width, and
359 $p = 0.3$ when, like in this case, $\frac{q}{\sqrt{gSD_{84}^3}} > 100$.

360

361 (3) Calculation of the Einstein dimensionless parameter:

362
$$\Phi = \frac{14\tau_{84}^{*2.5}}{\left[1 + \left(\frac{\tau_{c84}^*}{\tau_{84}^*} \right)^4 \right]}$$

363

364 (4) Calculation of the volumetric bedload transport rate ($\text{m}^3 \text{ s}^{-1}$):

365
$$q_{sv} = w \sqrt{g(s-1)D_{84}^3} \Phi$$

366 where w is the bankfull width (m) and s is the relative sediment density, i.e., the ratio of sediment
367 density to flow density (=2.65).

368

369 The data needed to calculate volumes are:

370 ▪ The bed slope, computed from the LiDAR DEM. The reliability of the method was tested with
371 a set of RTK-DGPS low-water levels. The bed slope was surveyed in 2010 and 2011 in 37 sections
372 whose length was around 10 times the width of the active channel (length range: 320-900 m). The
373 LiDAR slope was slightly underestimated but close to the 1:1 line and the correlation with the DGPS
374 slope was strong and highly significant (LiDAR slope = 0.83 x DGPS slope + 0.0001; $R^2 = 0.83$, p-
375 value < 0.0001). Furthermore, the relation is similar to that obtained by Biron et al. (2013) ((LiDAR
376 slope = 0.91 x DGPS slope + 0.002; $R^2 = 0.75$), who concluded that the LiDAR slope can be
377 confidently used to compute stream power.

378 ▪ The bed width, obtained from GIS analysis and expressed by two parameters:
379 (i) bankfull width, which allows computation of the specific water discharge (water discharge
380 per unit width).
381 (ii) active channel width, which allows calculation of the total bedload discharge.

382 ▪ The grain-size distribution determined from photos as explained previously.

383 ▪ Daily discharges at Montluçon gauging stations for AUD and Saint-Amand-Montrond gauging
384 stations for the other sites (from <http://www.hydro.eaufrance.fr/>) (Figure 1).

385 In each site, several bedload volume estimations were obtained by applying the formula upstream
386 to PCs to different reach lengths equal to 12, 18, and 24 times the width of the active channel. The
387 slope, active channel width and bankfull width specific to each reach were used. The slope was
388 obtained from 2011 LiDAR DEM. The bankfull width was obtained from the ratio of the active
389 channel width to the bankfull width computed by Dépret et al. (2015). Different grain sizes were
390 tested. We used the mean grain size available for each reach, the grain size of the last bar just upstream
391 from the entrance to each PC, the grain size of the bar just downstream from the entrance to the PC,
392 and the mean grain size of all bars in all the PCs. Among these combinations, we retained the highest
393 bedload value. It was finally multiplied by two, as Recking et al. (2012) reported that at the decadal
394 scale, the formula provides reliable estimations within a factor envelope of two. For comparison with
395 the bedload volumes, the deposited volumes were corrected using porosity. Because field data were
396 missing, we chose two values (0.1 and 0.5), which represent the wide porosity spectrum encountered
397 in sand and gravel bed rivers (Frings et al., 2011; Liang et al., 2015; Tabesh et al., 2019).

398

399 Finally, we looked at the extent to which deposited material in PCs could have originated from the
400 upper reach via vertical or lateral erosion. As no topo-bathymetric data were available, we used low-
401 water elevation surveyed upstream from PCs from 1989-1995 to 2011-2016 as a proxy of vertical
402 erosion (Gurnell et al., 2003; Wyzga, 2007). These data were provided by DREAL Centre-Val-de-
403 Loire and different private engineering companies brought together for the purpose of 1D hydraulic
404 modelling of flood hazards. On a section of the river roughly equal to 60 times the bankfull width (3
405 km for AUD, 3.6 km for the five other sites), we estimated the volume of sediment supplied to the
406 riverbed by lateral erosion of the floodplain using the 2011 LiDAR as well as t_0 and 2011 aerial photos
407 (acquired in 2013 for AUD and in 2010 for PRE). In the first step, eroded surfaces between t_0 and
408 2011 were determined using GIS following the method applied by Dépret et al. (2015, 2017). In the
409 second step, their surface area was multiplied by the height of the floodplain above the riverbed. For
410 this purpose, we estimated the height of the floodplain above the water level along each of the eroded
411 surfaces, applying the method presented previously, to compare the height of deposits in the PCs and
412 height of the floodplain along the PCs. We then added +0.5 m to account for water depth (considered
413 as the mean water depth at low flow).

414

415 **3.3 Controlling variables of the recovery rates**

416 In theory, the planimetric recovery rate is mainly controlled by the original volume of the PC, the
417 volume of sediment originating from upstream and the trap efficiency of the PC. The smaller the
418 original volume, the bigger the supply of sediment, especially the bedload volume, and finally, the
419 more will be trapped in the PC, and the faster the recovery rate. To test this hypothesis, we examined
420 Spearman's correlation between the 2011 recovery rate and the ratio of the volume deposited in the
421 PCs to the original volume. This ratio expresses the three above-mentioned explanatory variables with
422 the deposited volume in PCs combining the influence of the amount of sediments supplied to PCs as
423 bedload or suspended load on one hand, and their trapping efficiency on the other hand. We used the
424 2011 recovery rate rather than the 2016 rate, because the explanatory variable we tested was obtained
425 from the 2011 LiDAR DEM.

426 The original volume was defined as the volume between the low-water level and the bedrock level
427 and was obtained by subtracting the low-water level DEM from the bedrock surface DEM. The low-
428 water level DEM was built from the 2011 LiDAR DEM, assuming the water level at low flow
429 remained constant from t_0 to 2011. This assumption seems to be confirmed by the comparison of low-
430 flow level upstream and downstream from the PCs (no data were available for the PCs) from the end
431 of the 1980s / beginning of 1990s which are clearly stable. In absence of topo-bathymetric data at t_0 ,
432 we used the bedrock elevation as reference. Here we assume that because the mining companies
433 wished to extract as much sediment as possible, they dug down to the bedrock. The bedrock elevation
434 was estimated along several sections thanks to GPR transects of the PCs at low flow in 2018 (Figure
435 3). GPR images were acquired with a MALA Ramac CUII (Mala geosciences) coupled with a 100
436 MHz shielded antenna to reduce unwanted reflections from trees in areas of alluvial forest (Neal,
437 2004). Topographical surveys were made with an RTK DGPS. GPR observations were recorded at an
438 in-line sampling interval of 0.2 m, a time window of 548 ns and a sampling frequency of 1079 MHz.
439 GPR data were processed with Reflex® software (Jol, 2009; Sandmaier, 2016). The processing flow
440 consisted of six steps. We started with static correction of the first arrival, which sometimes showed
441 irregularities. Then we de-wowed data to remove very low frequency components. Next, we applied a
442 gain correction and energy decay gain to preserve relative amplitude information. Data were then
443 filtered to remove low and high frequency noise using a band-pass Butterworth filter. A topographic
444 profile was then added to each profile to correct topographic effects. Finally, a time-depth conversion
445 was applied based on the diffraction hyperbola fitting (Santaniello et al., 2013). No velocity analysis
446 was performed during the field campaign. A specific velocity pattern was defined for each transect.
447 Velocity ranged from 0.065 m ns^{-1} to 0.095 m ns^{-1} . The dominant bedrock geology is sandy-clay for
448 AUD and BOU and limestone and clay for PRE, STH, SFL and BRU, so in all cases the dielectric
449 constant of the bedrock is higher than the dielectric constant of PC filling, thus we were able to
450 observe the bedrock upper boundary in the form of a more or less continuous reflector (Figure 4). In
451 some cases, the GPR signal was too weak to detect the upper boundary of the bedrock. This can be
452 explained by (1) a clayey deposit that weakened the GPR wave or (2) weathering of the upper part of
453 the bedrock so there was no obvious boundary. In the later case, we chose a discontinuous picking

454 method to map the bedrock upper boundary. The determination of bedrock elevation through GPR was
455 enabled by the existence of logs located near or in the vicinity of the PCs. Logs were reported by the
456 BSS-BRGM database belonging to the Mining and Geological Research Institute (*Bureau des*
457 *Recherches Géologiques et Minières*) and by the Centre for Studies and Expertise on Risks,
458 Environment, Mobility and Development (*Centre d'études et d'expertise sur les risques,*
459 *l'environnement, la mobilité et l'aménagement*, French acronym CEREMA). With the GIS, the
460 estimated elevations of the bedrock were then assigned to cross sections passing through each
461 measurement point and perpendicular to the central line. A 1-m resolution bedrock surface DEM was
462 then built from these cross sections.

463

464

465

466 **Figure 3** – Location of ground penetrating radar surveys of the six mined river reaches.

467

468

469

470 **Figure 4** – (A) 100 Mhz Ground Penetrating Radar (GPR) profile at BOU. The solid black line
471 represents the surface of the bedrock. (B) The GPR trace (the vertical dashed green line in A) shows
472 the negative-positive-negative reflection corresponding to the bedrock upper boundary (dashed red
473 line).

474

475 The volume deposited in the PCs was calculated by subtracting the 2011 LiDAR DEM from the
476 bedrock surface DEM. Such volumes are an underestimation of the actual volumes deposited because
477 submerged deposits could not be taken into account (the 2011 active channel was excluded from the
478 analysis). Furthermore, because of the reduction in the trap efficiency of PCs over time, the
479 longitudinal sediment connectivity may have been restored before the LiDAR survey, and some
480 deposited particles may have been remobilized and exported to downstream PCs.

481

482

483 **4. Results**

484 **4.1 Channel adjustments**

485 *Planimetric adjustments*

486 The changes in the width index indicate that the six sites have begun to recover as the index has
487 decreased since the end of gravel mining, which happened between 23 and 47 yr before the most
488 recent aerial photograph (2016) we used was taken (Figure 5A). Whereas it originally ranged between
489 1.71 and 3.66, in 2016, it was between 0.96 and 3.43. BOU has fully recovered with an index close to
490 one in 2016. Among the five others, four have a relatively low index, ranging from 1.17 to 1.40. Only
491 PRE, with an index that evolved from 3.66 in 1969 to 3.43 in 2016, has almost not recovered at all.

492 As shown by the annual percentage reduction in the original surface area, the recovery rate ranges
493 from 0.12 to 1.99% yr⁻¹ (AUD: 1.72%, BOU: 1.99%, BRU: 1.28%, SFL: 1.56%, STH: 1.52%, PRE:
494 0.12%). If we exclude PRE, the range is narrower, 1.28 to 1.99% yr⁻¹. As indicated by the very high
495 coefficients of determination of the linear regressions between the percentage of reduction with respect
496 to the original surface area and the time that has elapsed since the end of gravel mining, vegetation
497 encroachment evolves mainly at a linear rate (Figure 5B).

498

499

500

501 **Figure 5** – Changes in the width index (ratio of the width of the PC to the width of the control reach)
502 (A) and percentage of the original surface area occupied by riparian vegetation (B).

503

504 Nevertheless, the width index alone is not sufficient to characterise the degree of planimetric
505 adjustment. Although the Cher River is a single thread river, Fig. 6 shows that in 2016, all the sites are
506 occupied by two or more channels separated by relatively big islands at least for part of the year.
507 However, in the four sites (AUD, BOU, SFL, STH) that have recovered the most (based on changes in
508 the width index), a main channel was clearly visible in 2016. The other branches, currently functioning

509 as secondary or abandoned channels, are in the process of being filled and encroached by woody
510 riparian vegetation.

511

512

513 **Figure 6** – Extent of terrestrialization in 2016.

514

515 Overall, the longitudinal pattern of terrestrialization in 2016 mimics that of the longitudinal
516 variability of the original width (Figure 7 and Figure 8). Most of the 2016 terrestrialized surfaces are
517 located where the original width exceeds a threshold value roughly equal to twice the river bed width
518 along the control reach. Table 3 shows that along these sections, the percentage of the total
519 terrestrialized surface ranges from 69% to 86% depending on the PC. Lastly, except for AUD and
520 BOU, which are the two PCs that have recovered the most, and PRE, which has almost not recovered
521 at all, the 20% downstream part of the sites are the least readjusted (Figure 7).

522

523

524 **Figure 7** – Longitudinal pattern of the terrestrialized width from the end of mining until 2013-2016.

525 Only the years preceding major changes are shown.

526

527

528 **Figure 8** – Relationship between terrestrialized width in 2016 and original width.

529

530

531 **Table 3** – Percentage of terrestrialized area and of the length of PCs located where the original width
532 of the PCs is double the width of the reference bed upstream.

	AUD	BOU	BRU	SFL	STH	PRE
% of terrestrialized surface	93	96	69	82	89	95
% of PC length	71	87	38	51	46	76

533

534

535 *Vertical adjustments*

536 In 2011, the mean elevation of sediment accumulations (bare and vegetated surfaces) above the
537 low-water level ranged between 0.4 and 1.2 m, corresponding to rates of between 0.009 and 0.065 cm
538 yr⁻¹. This is much lower than the mean elevation of the floodplain, ranging from 2.5 to 4.1 m above the
539 low-water level (Table 4). Furthermore, the accumulation rate and the rate of planimetric change
540 (computed from bare and vegetated surfaces) in 2011 are not significantly correlated (Spearman
541 correlation test: $R^2 = 0.1$, $p = 0.54$), indicating different trajectories of change at the different mining
542 sites.

543

544 **Table 4** – Mean elevation (m) of sediment accumulation above the low-water level in PCs (bare and
545 vegetated surfaces) and of the floodplains in 2011 (in m above the low-water level).

	AUD	BOU	BRU	SFL	STH	PRE
PC	0.8	0.9	0.6	1.2	1.0	0.4
Floodplain	2.5	4.0	4.1	4.0	3.7	2.8

546

547

548 Concerning the longitudinal pattern, we first expected that the relative depth of the sediment
549 accumulation would decrease downstream, and second that the higher the planimetric evolution rate
550 and the more advanced the recovery, the smaller the downstream decrease in sediment accumulation
551 would be. However, as indicated by the black curve in Figure 9, such a decrease in downstream
552 accumulation was only observed in AUD and BOU, which are the two PCs that have recovered the
553 most from a planimetric point of view (Figure 5B). In the four others PCs, accumulation increased
554 slightly downstream, but the trend was only statistically significant in PRE (Figure 9).

555

556

557

558 **Figure 9** – Longitudinal pattern of sediment elevation above the low-water level in 2011.

559
560
561
562
563
564
565
566
567
568
569
570
571
572
573
574
575
576
577
578
579
580
581
582
583
584
585
586

Grain-size adjustments

Except in PRE, where only one bar was established, and except for D₉₅ in SFL, there was a decreasing downstream trend in D₅₀ or D₉₅ that seems to indicate that grain-size adjustment is ongoing (Figure 10). The rate of decrease was even higher when the range of grain size in the PC was wide, pointing to a probable role for the range of available grain size upstream from the PCs. What is more, the rate was very low in BRU and SFL. All sites considered, the decrease was nevertheless only statistically significant for both D₅₀ and D₉₅ in AUD and BOU. It was also significant for D₅₀ in SFL and in STH (but only for the Wolman samples in STH).

The D₅₀ ranged from very fine or fine to medium gravels in BOU, BRU, SFL and PRE (respectively 8-17 mm, 4-11 mm, 3-11 mm, 3-12 mm) and from very fine or fine to very coarse gravels in AUD and STH (respectively, 2-42 mm and 7-47 mm).

Three distinct situations can be highlighted concerning the upstream and downstream context. In AUD, bedload transport appears to be relatively active and sediment availability quite high: the density of alluvial riffles and bars upstream/downstream from the PC was high (see spacing of riffle and bars in Table 5) and the grain-size along these two reaches resembled that of the PC (Figure 10). The minimum D₅₀ in the PC is nevertheless much lower than the minimum D₅₀ upstream/downstream. In the case of BOU and BRU, the density of riffles and bars in the upstream reach was much higher than in the downstream reach (Table 5 and Figure 10). Furthermore, the minimum D₅₀ in the PC was close to the minimum D₅₀ upstream/downstream. The upstream grain-size trend in BOU and BRU nevertheless clearly differed, as it was relatively stable in BOU but underwent a marked decrease in BRU. Then in SFL, STH and PRE, bed sediment availability, and hence likely bedload transport, appeared to be very low as demonstrated by the absence or almost complete absence of bars and alluvial riffles (Table 5 and Figure 10).

Figure 10 – Longitudinal grain-size pattern (D₅₀ and D₉₅) in and around PCs.

587 **Table 5** – Mean distance (in metres normalised by the active bed width in the control reaches)
 588 between riffles and bars in the PCs and along their upstream or downstream control reaches (computed
 589 on a length equal to that of the PCs) in 2018.

		AUD	BOU	BRU	SFL	STH	PRE
Riffle	PC	5	11	7	17	7	NA
	Control reach	10	9	NA	NA	NA	NA
Bar	Control reach	5	5	10	NA	33	NA

590

591

592 **4.2 Size and origin of deposited sediments**

593 *Size of the infilling sediments*

594 The trap efficiency formula indicates that at t_0 , all PCs trapped all particles coarser than medium
 595 (0.25 mm) or coarse sand (0.5 mm), depending on the PC, and consequently the entire bedload (Fig.
 596 S1). The trap efficiency for particles finer than medium silt (16 μm) was almost zero whatever the
 597 discharge considered. The trap efficiency for coarse silts (32 μm) was very low at almost all
 598 discharges. All these observations imply that at t_0 , most of the sandy fraction of the suspended load
 599 was deposited in the PCs and that conversely, most of the silty fraction was flushed through.

600

601

602 **Figure S1** – Trap efficiency from very fine silt (4 μm) to medium sand (0.25 mm). Whatever the
 603 discharge considered, the trap efficiency of particles coarser than medium sand reached 100%.

604

605 Compared with the volumes deposited in the PCs, the estimated maximum bedload volume were
 606 low in the three upstream PCs (AUD, BOU and BRU), and much higher in the three downstream ones
 607 (SFL, STH and PRE) (Table 6). This indicates that, at least in the case of AUD, BOU and BRU, a
 608 large proportion of the deposited material was transported into the PCs by uniform or graded
 609 suspension and is thus composed of silt and/or sand.

610

611 **Table 6** – Original volumes of PCs, deposited volumes in 2011 in PCs in 2011, maximum bedload
 612 volumes supplied to PCs from t_0 to 2011 (m^3), and maximum volumes delivered from the riverbed
 613 adjustment upstream to PCs by lateral erosion and by possible bed degradation from t_0 to 2011.

	AUD	BOU	BRU	SFL	STH	PRE
Original vol. of PCs	347,050	336,050	493,400	163,500	267,500	447,250
Deposited vol. in PCs in 2011	255,900	280,950	139,500	100,000	149,400	22,600
Max. bedload vol.	13,900	19,250	18,900	1,363,050	576,050	85,800
Upstream laterally eroded vol.	81,700	59,950	20,100	700	73,350	0
Upstream degraded vol.	29,750	34,350	41,550	32,500	31,200	35,900
Laterally eroded + Degraded vol.	111,450	94,300	61,650	33,200	104,550	35,900
Ratio of maximum bedload volumes / deposited vol. (porosity 0.5)	0.11	0.14	0.27	25	7.69	7.69
Ratio of maximum bedload volumes / deposited vol. (porosity 0.1)	0.06	0.08	0.15	14.29	4.35	4.17
Ratio of laterally eroded vol. / deposited vol.	0.32	0.21	0.14	0.01	0.49	0.00
Ratio of degraded vol. / deposited vol.	0.12	0.12	0.30	0.32	0.21	1.59
Ratio of total reinjected vol. / deposited vol.	0.44	0.34	0.44	0.33	0.70	1.59

614

615

616 A good example of the major role played by fine sediments in the infilling of the PCs, and their
 617 geomorphic recovery, is BOU, where the percentage of sediment size lower than 1 mm, considered as
 618 the approximate limit between bedload and suspension, was roughly estimated (Figure 11). We
 619 identified two main types of deposits located in distinct areas when we examined the five longitudinal
 620 profiles surveyed along the PC. The resistivity of the deposits located on the right-hand bank in the
 621 upstream half of the PC (P4 ERT profile) was very high (median 1435 Ω m) and the proportion of
 622 sediments < 1 mm was relatively low (35%). In the rest of the PC, resistivity decreased considerably
 623 (median between 101 Ω m and 182 Ω m for P10, P11, P12 and P13) and the proportion of sediments <

624 1 mm increased significantly (70%, 58%, 71% and 61% for P10, P11, P12 and P13, respectively)
625 (Figure 12). Finally, particles < 1 mm were estimated to account for 56% of the total deposited
626 volumes in 2011.

627

628 **Figure 11** – Relation between resistivity and percentage of sediment volume < 1 mm in BOU.

629

630

631 **Figure 12** – Electrical resistivity tomography in BOU.

632

633 *Upstream delivery*

634 Only a relatively small fraction of the deposited volumes can have originated from vertical or
635 lateral erosion of the upstream reach. The hypothesis of a PC being infilled because of a massive
636 sediment supply from headward erosion can very likely be rejected because the comparison of the
637 low-water level upstream from the PCs from the end of the 1980s / beginning of 1990s until the early
638 2010s was clearly stable, except for SFL1 located 4 km upstream from the entrance of SFL (Fig. S2).
639 In PRE, mining ended in 1969 so the vertical evolution of the bed for the first 20 yr following mining
640 could not be characterised. A bias associated with the comparison of low-water levels is nevertheless
641 possible, as a slight bed degradation (up to 0.1-0.2 m) might have not been detected using this method
642 and/or the few available points of comparison might not be representative of the vertical changes to
643 the riverbed upstream from the PCs. If we consider a 0.2 m bed degradation upstream from the PCs
644 over a river reach equal to 60 times the bankfull width (3 km for AUD, 3.6 km for the other PCs)
645 between t_0 and 2011 and if we consider that the whole degraded volume was trapped by PCs over the
646 study period, we obtain a very low ratio between the degraded volume and the deposited volume
647 (Table 6). Only PRE might have been filled by sediment originating from bed degradation, mainly
648 because its deposited volume is very small. The values of the ratios are nonetheless overestimated
649 because the deposited volumes in PCs are underestimated and the degraded volumes are probably also
650 overestimated. A similar conclusion can be drawn concerning lateral erosion in the upstream reach
651 (Table 6). The volumes involved are indeed much smaller than the infilled volumes. Furthermore,

652 whereas we considered that all the laterally reinjected volumes reached the PCs, in fact, part of the
653 volume is very likely stored in the riverbed upstream from the PCs (Table 6), as indicated by the many
654 newly created areas colonized by vegetation upstream from the PCs between t_0 and 2011, especially in
655 AUD, BOU, BRU and STH. Taking the degraded and the laterally eroded volumes together, the
656 findings remain the same (Table 6).

657

658

659 **Figure S2**– Changes in the low-water level between 1989 and 2016 in the reach located upstream
660 from the gravel pits (Minimum monthly discharge: $3.4 \text{ m}^3 \text{ s}^{-1}$ for AUD and $7.1 \text{ m}^3 \text{ s}^{-1}$ for the other
661 sites).

662

663 **4.2 Controlling factors**

664 The overall planimetric recovery rate was highly and significantly correlated with the deposited
665 volume / original volume ratio ($R^2 = 0.89$; $p\text{-value} = 0.0048$), thus confirming our initial assumption of
666 a recovery rate controlled by the original volume of PCs, by the volume of sediment supplied from
667 upstream and by the trap efficiency of the PCs.

668

669

670

671 **Figure 13** – Relationship between 2011 planimetric recovery rate and the ratio between the deposited
672 volume in 2011 and the original volume.

673

674

675 **5. Discussion**

676 **5.1 The role of suspended load and bedload in the recovery rates**

677 Our results indicate that at least in the three upstream PCs (AUD, BOU, BRU), the filling material
678 is only partially composed of bedload sediments (Table 6). In contrast, in the three downstream PCs
679 (SFL, STH and PRE), all the filling originated from bedload, because the deposited volumes are

680 clearly lower than the bedload supply computed using Recking's formula (Table 6). This observation
681 nevertheless seems quite paradoxical given the apparent limited bed sediment availability upstream
682 from these PCs, as indicated by the total absence of bars and alluvial riffles (Figure 10 and Table 5).
683 This absence does not seem to be the expression of the progression of a headward erosion front from
684 PCs since the beginning of mining because bars are also rare in aerial photos acquired before sediment
685 mining began. This is evidence for strongly limited transport conditions and overestimation of the
686 maximum bedload volumes obtained from grain-size in the PCs. The paradox is even more striking
687 when we compare the bedload volumes in the three upstream and the three downstream PCs. In SFL,
688 STH and PRE, the maximum bedload estimations are respectively between 88 and 163, 27 and 50, and
689 2 and 5 times higher than in the three upstream PCs. Yet, in contrast to the downstream PCs, the
690 reaches located immediately upstream from the three upstream PCs show a relative abundance of bars
691 and alluvial riffles, suggesting active bedload transport (Figure 10 and Table 5). Expressed in terms of
692 specific transport rates, the bedload was between $0.52 \text{ t km}^2 \text{ yr}^{-1}$ and $0.58 \text{ t km}^2 \text{ yr}^{-1}$ for the three
693 upstream PCs whereas it was $46.7 \text{ t km}^2 \text{ yr}^{-1}$, $13.9 \text{ t km}^2 \text{ yr}^{-1}$ and $1.3 \text{ t km}^2 \text{ yr}^{-1}$ for SFL, STH and PRE,
694 respectively. The values for the three upstream PCs and PRE are in agreement with those provided by
695 Houbrechts et al. (2008) for 16 rivers flowing in a relatively similar climatic and geological context,
696 which range from $0.3 \text{ t km}^2 \text{ yr}^{-1}$ to $2.8 \text{ t km}^2 \text{ yr}^{-1}$ (periods: 2-31 yr, watershed areas: 0.26-2691 km²,
697 bankfull specific stream power: 17-140 W m⁻²). In contrast, the bedload rates for SFL and STH are
698 extremely unlikely, because they are close to the highest rates reported worldwide, and exceed several
699 tens of $\text{t km}^2 \text{ yr}^{-1}$ (e.g., Powell et al., 1996; Rickenmann, 1997; Ziegler et al., 2014). If we apply a rate
700 of $0.6 \text{ t km}^2 \text{ yr}^{-1}$ to SFL and STH, i.e., the maximum estimated rate amongst the three upstream PCs,
701 we obtain bedload volumes between 2.9 and 5.4 times lower than the deposited volumes. All the
702 above-mentioned considerations suggest that the filling material in SFL and STH is only partially
703 composed of bedload sediments. Lastly, only PRE could have been completely filled with bedload
704 because if we apply the same correction as the one we used for SFL and STH, the deposited volume is
705 2-3.6 times lower than that of the bedload. Nevertheless, considering that the specific stream power
706 upstream to PRE is the lowest amongst the six PCs and that the maximum D_{50} in PRE is 3 mm, it can
707 reasonably be hypothesised that the deposited volume is partly composed of suspended load. Finally,

708 the importance of the suspended load in the recovery potential of PCs is emphasised by assuming 56%
709 of the deposited volume in BOU in 2011 was made up of particles < 1 mm, as estimated from the
710 combination of geophysical surveys and grain-size analysis (Figure 11 and Figure 12). If we consider
711 this grain size as a rough limit between bedload and suspended load processes, this implies that only
712 44% of the infilled volume in BOU can be attributed to bedload transport.

713

714

715

716 **5.2 The influence of the sand load on the recovery processes**

717 Whatever the PC considered, a large proportion of the deposited volume comprised of particles < 2
718 mm is hypothesised to be sand. At t_0 , the trap efficiency for silt would be almost null for particles smaller than medium silt and very low for coarse silt. Furthermore, because of the progressive infilling of the PCs, trap efficiency in submerged areas decreases over time (Verstraeten and Poesen, 2000). As long as a PC remains submerged, silt is highly unlikely to be deposited. However, once the deposits emerge at low flow and have begun to be encroached by vegetation, the trap efficiency for suspended load is hypothesised to become significant (Corenblit et al., 2007; 2020). Trap efficiency on these elevated vegetated surfaces should thus result in a thick layer of silty material, transported as a uniform suspended load in the upper part of the water column. Yet, comparing the elevation in the 2011 LiDAR data and the DGPS data acquired in 2019 along the ERT survey sections in BOU on surfaces colonized by vegetation in 2011 shows almost complete absence of aggradation and thus probably a low silty load in the Cher River. For this comparison, we selected LiDAR points located less than 20 cm from DGPS points (giving a total of 526 points). Our comparison shows that for 75% of the paired points, the absolute difference in elevation is lower than the total error in elevation measurement (equal to 0.096 m and computed as proposed by Taylor (1997) when different components of a total error are considered as independent and are assumed to follow a Gaussian distribution:

734 $\sqrt{E_{DGPS}^2 + E_{LiDAR}^2}$, with E_{DGPS}^2 the DGPS vertical error and E_{LiDAR}^2 the LiDAR vertical error equal to

735 the mean absolute difference from control points). Moreover, the difference in 95% of the paired
736 points is less than 0.2 m. Most of the suspended material and hence a large proportion of the total
737 volume deposited in PCs is consequently hypothesised to be mainly composed of sand. Transported as
738 a uniform suspension for its finest grain-size fraction, or as a graded suspension or as bedload (at low
739 discharges) for its coarsest fraction, sand is therefore hypothesised to be the main determining factor in
740 the morpho-sedimentary recovery potential of PCs in the Cher River. Furthermore, the role of sand in
741 the recovery process probably goes even further because, at least up to a certain threshold (40% in
742 Miwa and Parker, 2017, 50% in Dudill et al., 2018), the sand content increases gravel mobility, which,
743 in turn, increases the bedload rate (e.g., Jackson and Beschta, 1984; Iseya and Ikeda, 1987; Wilcock et
744 al., 2001; Curran and Wilcock, 2005; Miwa and Parker, 2017; Perret et al., 2018; Dudill et al., 2018).
745 Such an effect is especially important in gravel-bed low-energy rivers as most of bedload very likely
746 occurs under partial transport conditions, namely with shear stress barely higher than the critical shear.
747 This implies that the role of gravels in the PCs recovery rates increases with an increase in the
748 proportion of sand in the subsurface layer. For example, compared to a river deprived of, or with a
749 very low sand content, the gravel mobility in the Cher River has very probably risen because the sand
750 content is between 22% and 28% (Dépret, 2014). Broadly, the volume of sand load can be considered
751 as a major control of the geomorphic recovery capacity of low energy gravel-bed systems.

752

753 **5.3 The need to account for the lithology when assessing recovery potential**

754 In addition, the role of the sand load in the Cher River PCs recovery highlights the importance of
755 watershed lithology in recovery potential. As exemplified by Macaire et al. (1997, 2001, 2002, 2013),
756 the amount of sand flux is strongly controlled by the lithological composition of the watershed.
757 Macaire et al. (1997, 2001, 2002) studied the Holocene sediment yield and flux in two small
758 lithologically contrasted basins in the Loire watershed, considered to be representative of the two main
759 lithological units that make up the Loire watershed (like the Cher River), the Massif Central upstream
760 and the Parisian Basin downstream. Macaire et al. (1997, 2001) showed that the total specific sediment
761 yield and the total amount of sediment flowing out of the Chambon watershed, located in the Massif
762 Central and mainly composed of granite, metamorphic and volcanic rocks, are largely dominated by a

763 solid load at the expense of a dissolved load. The opposite was reported for the Négron watershed,
764 located in the Parisian Basin and mainly composed of Cenomanian sand and marl, Oxfordian
765 limestone and marl as well as of Turonian chalk (Macaire et al., 2001, 2002). Extrapolating their
766 results to the whole Loire basin, Macaire et al. (2001) estimated that 91% of the total solid yield
767 originated from the Massif Central. The remaining 9% would thus have been produced in the
768 sedimentary context of the Parisian Basin. The minor role played by the Parisian Basin in the sediment
769 delivery is supported by the very low proportion of sand originating from sedimentary rocks in the
770 path of the Loire River through the Parisian Basin (Macaire et al., 2013). This means that if the
771 lithology of the Cher watershed had been dominated by limestone, especially in its upper part, the sand
772 load, and hence the recovery rate of the PCs, would have been much lower. It also implies that the
773 recovery capacity of low-energy gravel-bed rivers increases with an increase in sand content and thus
774 unquestionably depends on the geological context. Finally, it stresses the need for low-energy rivers to
775 include watershed lithology when designing a recovery plan that incorporates morpho-sedimentary
776 aspects. The same maintenance or restoration practices can indeed lead to significantly different
777 results depending on the watershed lithology.

778

779 **5.4 The role of PCs in habitat diversity**

780 Shifting riverscape mosaic processes are known to trigger rejuvenation of riparian successions
781 associated with pulse disturbance and their conservation or restoration is an issue in biodiversity
782 conservation (e.g., Stanford et al., 2005; Tockner et al., 2010; Hauer et al., 2016; Diaz-Redondo et al.,
783 2018;). The Cher River has been subject to longstanding anthropogenic inhibition of lateral mobility
784 that has strongly limited such processes (Dépret et al., 2015, 2017; Vayssière et al., 2016, 2020).
785 Moreover, its riparian forest, currently composed of a thin discontinuous strip, is in a remnant state
786 because of the pressure exerted by farming and pasture in the floodplain. What is more, the riparian
787 forest is also threatened by the drop in the alluvial water table caused by the bed incision (up to 2.5 m
788 in some reaches) that followed gravel mining (Dépret, 2014). In this context, PCs play a paradoxical
789 role. Drivers of the bed incision, and thus partly responsible for the deterioration of riparian forests,
790 PCs are nevertheless currently transient hotspots for riparian diversity, in particular, by allowing

791 pioneer vegetation to encroach. This is apparent when one compares the surface of newly deposited
792 bars available for vegetation colonization inside the PCs and outside. The latter data are available
793 between BRU and Vierzon for the period 1959-2016. Along this reach, the area of deposited surfaces
794 colonized by vegetation in the PCs (BRU, SFL, STH, PRE and two others not included in the present
795 study) represents 35% of the total area of deposited surfaces along this reach, whereas their course
796 occupies only 10% of the total length of the river. Managers should thus pay particular attention to
797 these woody pioneer habitats located inside the PCs. Nonetheless, their ecological benefits could be
798 short lived because they are not able to self-maintain. With the progressive aggradation of their
799 surfaces, which reduces stresses caused by flooding and increases the depth of the water table, the
800 pioneer habitats will inevitably evolve towards the mature stage dominated by hardwood species
801 similar to those composing the remnant riparian forest in the floodplain. The question remains of when
802 this succession will occur. The almost complete absence of aggradation observed in BOU between
803 2011 and 2019 on surfaces occupied by pioneer vegetation (reported in Section 5.2) as well as the
804 thinness of the layer of silty deposits on these surfaces suggest that the establishment of a hardwood
805 forest could take at least a few decades starting now. A similar issue of sustainability applies to the
806 aquatic habitats. PCs also increase their heterogeneity because of the creation of abandoned channels
807 and to the diversification of geomorphic units (riffles, pools and bars), especially in the three
808 downstream PCs surrounded by reaches that are almost completely deprived of such units (Fig. 10 and
809 Table 4).

810

811

812 **6. Conclusion**

813 This study investigated the recovery of a low energy gravel-bed river more than 20 yr after gravel
814 mining ended. Our specific objectives were to describe and quantify the morpho-sedimentary
815 readjustment of extended and over-widened mining pits (we named pseudo-captures) and to identify
816 the factors that control their recovery rate, which we defined using criteria of perennial vegetation
817 encroachment. Thanks to an interdisciplinary methodological approach, we identified a wide spectrum
818 of recovery magnitude closely correlated with the ratio of the volume of sediment deposited in pits to

819 their volume when mining ended. In addition, we demonstrated that the infilled material is only partly
820 composed of bedload and consequently that the suspended load, mainly sand, plays the main role in
821 the recovery process. Whereas the watershed is separated into two main lithological units, with
822 crystalline and metamorphic rocks upstream and sedimentary rocks downstream, most of the sand is
823 assumed to have originated from the upper watershed, highlighting the importance of the surficial
824 lithology in the recovery potential. The abundance of sand explains the unexpectedly high recovery
825 rate of some pseudo-captures despite the low energy of the river. Our results highlight the need to
826 further improve our knowledge in the morphogenic role of sand in gravel-bed rivers. Progress is
827 required particularly in quantifying the proportion of sand in the total solid load of rivers as well as in
828 identifying the conditions under which it is transported as suspended material or as bedload.
829 Measuring fluxes remains a complex task and methods to achieve it are still rare and those that exist
830 are associated with high uncertainty particularly because of the spatio-temporal variability at which the
831 sand-size classes flows in suspension or as bedload (Camenen et al., 2019). Lastly, from a
832 methodological point of view, our study illustrates how our understanding of geomorphic processes
833 can be improved by the combined use of standard geomorphological methods, which mainly provide
834 information concerning surface changes (grain-size, topography, planimetry, etc.), and the use of
835 geophysical methods such as ground penetrating radar or electrical resistivity tomography, which
836 make it possible to investigate the texture and structure of sediments beneath the surface.

837

838

839 **Acknowledgements**

840 This research was conducted in the framework of the *Plan Loire Grandeur Nature*. It was funded by
841 the FEDER *Bassin de la Loire* and the *Agence de l'Eau Loire-Bretagne*. The authors thank Anaëlle
842 Vayssière and Agnès Gauthier for their help with the core interpretation. Finally, the authors would
843 like to express their gratitude to the editor, Scott Lecce, to Lorenzo Marchi and to a second
844 anonymous reviewer for their constructive comments and suggestions that have significantly improved
845 this paper.

846

847

848 **References**

- 849 Arróspide, F., Mao, L., Escauriaza, C., 2018. Morphological evolution of the Maipo River in central
850 Chile: Influence of instream gravel mining. *Geomorphology* 306, 182–197.
851 <https://doi.org/10.1016/j.geomorph.2018.01.019>
- 852 Barman, B., Kumar, B., Sarma, A.K., 2019. Dynamic characterization of the migration of a mining pit
853 in an alluvial channel. *International Journal of Sediment Research* 34, 155–165.
854 <https://doi.org/10.1016/j.ijsrc.2018.10.009>
- 855 Barman, B., Kumar, B., Sarma, A.K., 2018. Turbulent flow structures and geomorphic characteristics
856 of a mining affected alluvial channel: Turbulence in Mining Affected Alluvial Channel. *Earth Surf.*
857 *Process. Landforms* 43, 1811–1824. <https://doi.org/10.1002/esp.4355>
- 858 Barman, B., Sharma, A., Kumar, B., Sarma, A.K., 2017. Multiscale characterization of migrating sand
859 wave in mining induced alluvial channel. *Ecological Engineering* 102, 199–206.
860 <https://doi.org/10.1016/j.ecoleng.2017.02.021>
- 861 Belletti, B., Nardi, L., Rinaldi, M., 2016. Diagnosing problems induced by past gravel mining and
862 other disturbances in Southern European rivers: the Magra River, Italy. *Aquat Sci* 78, 107–119.
863 <https://doi.org/10.1007/s00027-015-0440-5>
- 864 Biron, P.M., Choné, G., Buffin-Bélangier, T., Demers, S., Olsen, T., 2013. Improvement of streams
865 hydro-geomorphological assessment using LiDAR DEMs. *Earth Surf. Process. Landforms* 38, 1808–
866 1821. <https://doi.org/10.1002/esp.3425>
- 867 Bravard, J. P., Amoros, C., Pautou, G., Bornette, G., Bournaud, M., Peiry, J.-L., Perrin, J. F., Tachet,
868 H., 1997. River incision in south-east France: morphological phenomena and ecological effects. *River*
869 *Res. Applic.* 13, 75-90.

870 Bravard, J. P., Kondolf, G.M., Piégay, H., 1999a. Environmental and societal effects of channel
871 incision, and remedial strategies. In: Darby, S.E., Simon, A. (Eds.), *Incised River Channels: Processes,*
872 *Forms, Engineering and Management.* John Wiley & Sons, Chichester, pp. 303–341.

873 Bravard, J.-P., Landon, N., Peiry, J.-L., Piégay, H., 1999b. Principles of engineering geomorphology
874 for managing channel erosion and bedload transport, examples from French rivers. *Geomorphology*
875 31, 291–311. [https://doi.org/10.1016/S0169-555X\(99\)00091-4](https://doi.org/10.1016/S0169-555X(99)00091-4)

876 Brown, A.V., Lyttle, M.M., Brown, K.B., 1998. Impacts of Gravel Mining on Gravel Bed Streams 16.

877 Bull, W.B., Scott, K.M., 1974. Impact of mining gravel from urban stream beds in the Southwestern
878 United States. *Geology* 1974 (2), 171–174.

879 Calle, M., Alho, P., Benito, G., 2017. Channel dynamics and geomorphic resilience in an ephemeral
880 Mediterranean river affected by gravel mining. *Geomorphology* 285, 333–346.
881 <https://doi.org/10.1016/j.geomorph.2017.02.026>

882 Camenen, B., Naudet, G., Dramais, G., Le Coz, J., Paquier, A., 2019. A multi-technique approach for
883 evaluating sand dynamics in a complex engineered piedmont river system. *Sci. Total Environ.* 657,
884 (485-497). <https://doi.org/10.1016/j.scitotenv.2018.11.394>

885 Cao, Z., Pender, G., 2004. Numerical modelling of alluvial rivers subject to interactive sediment
886 mining and feeding. *Advances in Water Resources* 27, 533–546.
887 <https://doi.org/10.1016/j.advwatres.2004.02.017>

888 Chen, D., Acharya, K., Stone, M., 2010. Sensitivity Analysis of Nonequilibrium Adaptation
889 Parameters for Modeling Mining-Pit Migration. *J. Hydraul. Eng.* 136, 806–811.
890 [https://doi.org/10.1061/\(ASCE\)HY.1943-7900.0000242](https://doi.org/10.1061/(ASCE)HY.1943-7900.0000242)

891 Church, M., Mclean, D.G., Wolcott, J.F., 1987. River bed gravels: Sampling and analysis. In: Thorne,
892 C.R., Bathurst, J.C., Hey, R. (Eds.), *Sediment transport in gravel-bed rivers.* Wiley & Sons,
893 Chichester, pp. 43-79.

894 Collins, B.D., Dunne, T., 1989. Gravel transport, gravel harvesting, and channel-bed degradation in
895 rivers draining the Southern Olympic mountains, Washington. U.S.A. Environ. Geol. Water Sci. 13,
896 213–224.

897 Comiti, F., Da Canal, M., Surian, N., Mao, L., Picco, L., Lenzi, M.A., 2011. Channel adjustments and
898 vegetation cover dynamics in a large gravel bed river over the last 200years. *Geomorphology* 125,
899 147–159. <https://doi.org/10.1016/j.geomorph.2010.09.011>

900 Corenblit, D., Tabacchi, E., Steiger, J., Gurnell A.M., 2007. Reciprocal interactions and adjustments
901 between fluvial landforms and vegetation dynamics in river corridors: A review of complementary
902 approaches. *Earth-Science Reviews* 84, 56–86. <https://doi.org/10.1016/j.earscirev.2007.05.004>

903 Corenblit, D., Vautier, F., González, E., Steiger, J., 2020. Formation and dynamics of vegetated fluvial
904 landforms follow the biogeomorphological succession model in a channelised river. *Earth Surf.*
905 *Process. Landforms.* 45 (09), 2020-2035.

906 Curran, J.C., Wilcock, P.R., 2005. Effect of Sand Supply on Transport Rates in a Gravel-Bed Channel.
907 *J. Hydraul. Eng.* 131, 961–967. [https://doi.org/10.1061/\(ASCE\)0733-9429\(2005\)131:11\(961\)](https://doi.org/10.1061/(ASCE)0733-9429(2005)131:11(961))

908 David, M., Labenne, A., Carozza, J.-M., Valette, P., 2016. Evolutionary trajectory of channel
909 planforms in the middle Garonne River (Toulouse, SW France) over a 130-year period: Contribution
910 of mixed multiple factor analysis (MFAMix). *Geomorphology* 258, 21–39.
911 <https://doi.org/10.1016/j.geomorph.2016.01.012>

912 Debrand-Passard, S., Lablanche, G., Flamand, D., Cavelier, C., Desprez, N., Caudron, M., Lafage, M.,
913 1977a. Carte géologique de France (1/50000), feuille de Bourges (519). BRGM, Orléans.

914 Debrand-Passard, S., Desprez, N., Bos, P., Durand, E., Trautmann, F., Bambier, A., 1977b. Notice
915 explicative, carte géologique de France (1/50000), feuille de Bourges (519). BRGM, Orléans (45 p).

916 Dépret, T., 2014. Fonctionnement morphodynamique actuel et historique des méandres du Cher. Ph.
917 Thesis, Paris 1 – Panthéon-Sorbonne University.

918 Dépret, T., Gautier, E., Hooke, J., Grancher, D., Vermoux, C., Brunstein, D., 2015. Hydrological
919 controls on the morphogenesis of low-energy meanders (Cher River, France). *Journal of Hydrology*
920 531, 877–891. <https://doi.org/10.1016/j.jhydrol.2015.10.035>

921 Dépret, T., Gautier, E., Hooke, J., Grancher, D., Vermoux, C., Brunstein, D., 2017. Causes of planform
922 stability of a low-energy meandering gravel-bed river (Cher River, France). *Geomorphology* 285, 58–
923 81. <https://doi.org/10.1016/j.geomorph.2017.01.035>

924 Diaz-Redondo, M., Marchamalo, M., Egger, G., Magdaleno, F., 2018. Toward floodplain rejuvenation
925 in the middle Ebro River (Spain): From history to action. *Geomorphology* 317, 117–127. doi:
926 10.1016/j.geomorph.2018.05.014

927 Downs, P.W., Piégay, H., 2019. Catchment-scale cumulative impact of human activities on river
928 channels in the late Anthropocene: implications, limitations, prospect. *Geomorphology* 338, 88–104.
929 <https://doi.org/10.1016/j.geomorph.2019.03.021>

930 Dudill, A., Lafaye de Micheaux, H., Frey, P., Church, M., 2018. Introducing Finer Grains Into
931 Bedload: The Transition to a New Equilibrium. *J. Geophys. Res. Earth Surf.* 123, 2602–2619.
932 <https://doi.org/10.1029/2018JF004847>

933 Fredsoe, J., 1978. Natural backfilling of pipeline trenches. *J. Petrol. Technol.* 31 (10), 1–223.

934 Frings, R.M., Schüttrumpf, H., Vollmer, S., 2011. Verification of porosity predictors for fluvial sand-
935 gravel deposits: Porosity prediction. *Water Resour. Res.* 47. <https://doi.org/10.1029/2010WR009690>

936 Gill, M.A., 1994. Hydrodynamics of Mining Pits in Erodible Bed under Steady Flow. *Journal of*
937 *Hydraulic Engineering* 120, 1337–1348. [https://doi.org/10.1061/\(ASCE\)0733-
938 9429\(1994\)120:11\(1337\)](https://doi.org/10.1061/(ASCE)0733-9429(1994)120:11(1337))

939 Gob, F., Houbrechts, G., Hiver, J.M., Petit, F., 2005. River dredging, channel dynamics and bedload
940 transport in an incised meandering river (the River Semois, Belgium). *River Res. Applic.* 21, 791–804.
941 <https://doi.org/10.1002/rra.883>

942 Graf, W.L., 2006. Downstream hydrologic and geomorphic effects of large dams on American rivers.
943 *Geomorphology* 79, 336–360. <https://doi.org/10.1016/j.geomorph.2006.06.022>

944 Gurnell, A.M., Peiry, J.L., Petts, G.E., 2003. Using historical data in fluvial geomorphology. In:
945 Kondolf, M.G., Piégay, H. (Eds.), *Tools in Fluvial Geomorphology*. Wiley & Sons, Chichester, pp.
946 77–101.

947 Haan, C.T., Barfield, B.J., Hayes, J.C., 1994. *Design Hydrology and Sedimentology for Small*
948 *Catchments*. Academic Press, San Diego, Calif.

949 Hauer, F.R., Locke, H., Dreitz, V.J., Hebblewhite, M., Lowe, W.H., Muhfield, C.C, Nelson, C.R.,
950 Proctor, M.F., Rood, S.B., 2016. Gravel-bed river floodplains are the ecological nexus of glaciated
951 mountain landscapes. *Sci. Adv.* 2 (6), e1600026. doi: 10.1126/sciadv.1600026

952 Houbrechts, G., Hallot, É., Gob, F., Mols, J., Defechereux, O., Petit, F., 2008. Fréquence et
953 importance du charriage dans les rivières du Massif ardennais. *GPQ* 60, 241–251.
954 <https://doi.org/10.7202/017998ar>

955 Iseya, F., Ikeda, H., 1987. Pulsations in Bedload Transport Rates Induced by a Longitudinal Sediment
956 Sorting: A Flume Study Using Sand and Gravel Mixtures. *Geografiska Annaler. Series A, Physical*
957 *Geography* 69, 15–27. <https://doi.org/10.2307/521363>

958 Jackson, W.L., Beschta, R.L., 1984. Influences of Increased Sand Delivery on the Morphology of
959 Sand and Gravel Channels1. *JAWRA Journal of the American Water Resources Association* 20, 527–
960 533. <https://doi.org/10.1111/j.1752-1688.1984.tb02835.x>

961 Jol, H.M., 2009. *Ground penetrating radar theory and applications*. Elsevier, Amsterdam.
962 <https://doi.org/10.1016/B978-0-444-53348-7.X0001-4>

963 Julien, P.Y., 2010. *Erosion and sedimentation*, 2nd edition. Cambridge University Press, 390 p.

964 Koehnken, L., Rintoul, M.S., Goichot, M., Tickner, D., Loftus, A., Acreman, M.C., 2020. Impacts of
965 riverine sand mining on freshwater ecosystems: A review of the scientific evidence and guidance for
966 future research. *River Res Applic* 36, 362–370. <https://doi.org/10.1002/rra.3586>

967 Kondolf, G., 1994. Geomorphic and environmental effects of instream gravel mining. *Landscape and*
968 *Urban Planning* 28, 225–243. [https://doi.org/10.1016/0169-2046\(94\)90010-8](https://doi.org/10.1016/0169-2046(94)90010-8)

969 Kondolf, G.M., 1997. Hungry Water: Effects of Dams and Gravel Mining on River Channels.
970 *Environmental Management* 21, 533–551. <https://doi.org/10.1007/s002679900048>

971 Kornis, S., Laczay, I.A., 1988. Effects of extensive dredging on the river regime. *Int. Conf. on River*
972 *Regime*, Hydraulic Research Ltd., John Wiley and Sons, New York, N.Y.

973 Lablanche, G., 1994. Carte géologique de France (1/50000), feuille de Saint-Amand-Montrond (572).
974 BRGM, Orléans.

975 Lablanche, G., Marchand, D., Lefavarais-Raymond, A., Debrand-Passard, S., Gros, Y., Debégliia, N.,
976 Maget, P., Lallier, D., 1994. Notice explicative, carte géologique de France (1/50000), feuille de Saint-
977 Amand-Montrond (572). BRGM, Orléans (81 p).

978 Larue, J.-P., 1981. Les nappes alluviales de la vallée du Cher dans le bassin de Montluçon. *noroi* 111,
979 345–360. <https://doi.org/10.3406/noroi.1981.3972>

980 Larue, J.-P., 2011. Longitudinal profiles and knickzones: the example of the rivers of the Cher basin in
981 the northern French Massif Central. *Proceedings of the Geologists' Association* 122, 125–142.
982 <https://doi.org/10.1016/j.pgeola.2010.08.006>

983 Latapie, A., Camenen, B., Rodrigues, S., Paquier, A., Bouchard, J.P., Moatar, F., 2014. Assessing
984 channel response of a long river influenced by human disturbance. *CATENA* 121, 1–12.
985 <https://doi.org/10.1016/j.catena.2014.04.017>

986 Lee, H., Fu, D., Song, M., 1993. Migration of Rectangular Mining Pit Composed of Uniform
987 Sediments. *Journal of Hydraulic Engineering* 119, 64–80. [https://doi.org/10.1061/\(ASCE\)0733-](https://doi.org/10.1061/(ASCE)0733-9429(1993)119:1(64))
988 9429(1993)119:1(64)

989 Lehner, B., Liermann, C.R., Revenga, C., Vörösmarty, C., Fekete, B., Crouzet, P., Döll, P., Endejan,
990 M., Frenken, K., Magome, J., Nilsson, C., Robertson, J.C., Rödel, R., Sindorf, N., Wisser, D., 2011.
991 High resolution mapping of the world’s reservoirs and dams for sustainable river flow management.
992 *Frontiers in Ecology and the Environment* 9, 494–502. <https://doi.org/10.1890/100125>

993 Lespez, L., Viel, V., Rollet, A.J., Delahaye, D., 2015. The anthropogenic nature of present-day low
994 energy rivers in western France and implications for current restoration projects. *Geomorphology* 251,
995 64–76.

996 Liang, R., Schruoff, T., Jia, X., Schüttrumpf, H., Frings, R.M., 2015. Validation of a stochastic digital
997 packing algorithm for porosity prediction in fluvial gravel deposits. *Sedimentary Geology* 329, 18–27.
998 <https://doi.org/10.1016/j.sedgeo.2015.09.002>

999 Loke, M.H., 2000. Electrical imaging surveys for environmental and engineering studies: A practical
1000 guide to 2-D and 3-D surveys. Electronic version available from <http://www.terra-plus.com>

1001 Loke, M.H., Barker, R.D., 1996. Rapid least-squares inversion of apparent resistivity pseudosections
1002 by a quasi-Newton method 1. *Geophysical Prospecting* 44, 131–152.

1003 Macaire, J.-J., Bellemlih, S., Cocirta, C., De Luca, P., Di-Giovanni, C., Gay-Ovejero, I., 2001.
1004 Quantification des flux et des stocks solides holocènes dans le bassin de la Loire (France). *La Houille*
1005 *Blanche* 35–38. <https://doi.org/10.1051/lhb/2001086>

1006 Macaire, J.-J., Bossuet, G., Choquier, A., Cocirta, C., Luca, P.D., Dupis, A., Gay, I., Mathey, E.,
1007 Guenet, P., 1997. Sediment Yield During Late Glacial and Holocene periods in the Lac Chambon
1008 Watershed, Massif Central, France 17.

1009 Macaire, J.-J., Bellemlih, S., Di-Giovanni, C., De Luca, P., Visset, L., Bernard, J., 2002. Sediment
1010 yield and storage variations in the Négron River catchment (south western Parisian Basin, France)

1011 during the Holocene period. *Earth Surf. Process. Landforms* 27, 991–1009.
1012 <https://doi.org/10.1002/esp.388>

1013 Macaire, J.-J., Gay-Ovejero, I., Bacchi, M., Cocirta, C., Patryl, L., Rodrigues, S., 2013. Petrography of
1014 alluvial sands as a past and present environmental indicator: Case of the Loire River (France).
1015 *International Journal of Sediment Research* 28, 285–303. <https://doi.org/10.1016/S1001->
1016 [6279\(13\)60040-2](https://doi.org/10.1016/S1001-6279(13)60040-2)

1017 Malavoi, J.R., Garnier, C.C., Landon, N., Recking A., Baran, P., 2011. *Eléments de connaissance pour*
1018 *la gestion du transport solide en rivière*. Onema, 216 p.

1019 Miwa, H., Parker, G., 2017. Effects of sand content on initial gravel motion in gravel-bed rivers:
1020 Effects of sand content on initial gravel motion in gravel-bed rivers. *Earth Surf. Process. Landforms*
1021 42, 1355–1364. <https://doi.org/10.1002/esp.4119>

1022 Mossa, J., Marks, S.R., 2011. Pit Avulsions and Planform Change on a Mined River Floodplain:
1023 Tangipahoa River, Louisiana. *Physical Geography* 32, 512–532. <https://doi.org/10.2747/0272->
1024 [3646.32.6.512](https://doi.org/10.2747/0272-3646.32.6.512)

1025 Neyshabouri, S.A.A.S., Farhadzadeh, A., Amini, A., 2002. Experimental and field study of mining pit
1026 migration. *Int. J. Sediment Res.* 17(4), 323–333.

1027 Nilsson, C., 2005. Fragmentation and Flow Regulation of the World's Large River Systems. *Science*
1028 308, 405–408. <https://doi.org/10.1126/science.1107887>

1029 Ollero, A., 2010. Channel changes and floodplain management in the meandering middle Ebro River,
1030 Spain. *Geomorphology* 117, 247–260. <https://doi.org/10.1016/j.geomorph.2009.01.015>

1031 Perret, E., Berni, C., Camenen, B., Herrero, A., El Kadi Abderrezzak, K., 2018. Transport of
1032 moderately sorted gravel at low bed shear stresses: The role of fine sediment infiltration. *Earth Surf.*
1033 *Process. Landforms* 43, 1416–1430. <https://doi.org/10.1002/esp.4322>

1034 Powell, D.M., Reid, I., Laronne, J.B., Frostick, L., 1996. Bed load as a component of sediment yield
1035 from a semiarid watershed of the northern Negev 9. Suite

1036 Recking, A., 2013. Simple Method for Calculating Reach-Averaged Bed-Load Transport. *J. Hydraul.*
1037 *Eng.* 139, 70–75. [https://doi.org/10.1061/\(ASCE\)HY.1943-7900.0000653](https://doi.org/10.1061/(ASCE)HY.1943-7900.0000653)

1038 Recking, A., 2010. A comparison between flume and field bed load transport data and consequences
1039 for surface-based bed load transport prediction. *Water Resour. Res.* 46.
1040 <https://doi.org/10.1029/2009WR008007>

1041 Recking, A., Liébault, F., Peteuil, C., Jolimet, T., 2012. Testing bedload transport equations with
1042 consideration of time scales. *Earth Surf. Process. Landforms* 37, 774–789.
1043 <https://doi.org/10.1002/esp.3213>

1044 Rempel, L.L., Church, M., 2009. Physical and ecological response to disturbance by gravel mining in
1045 a large alluvial river. *Can. J. Fish. Aquat. Sci.* 66, 52–71. <https://doi.org/10.1139/F08-184>

1046 Rickenmann, D., 1997. Sediment transport in Swiss torrents. *Earth Surf. Process. Landforms* 22, 937–
1047 951.

1048 Rinaldi, M., Wyżga, B., Surian, N., 2005. Sediment mining in alluvial channels: physical effects and
1049 management perspectives. *River Res. Applic.* 21, 805–828. <https://doi.org/10.1002/rra.884>

1050 Rollet, A.-J., Piégay, H., Citterio, A., 2008. Impact des extractions de graviers dans le lit mineur sur la
1051 géométrie des zones aquatiques périfluviales du Doubs (France). *Geogr. Phys. Quat.* 60, 253–269.
1052 <https://doi.org/10.7202/017999ar>

1053 Rovira, A., Batalla, R.J., Sala, M., 2005. Response of a river sediment budget after historical gravel
1054 mining (the lower Tordera, NE Spain). *River Res. Applic.* 21, 829–847.
1055 <https://doi.org/10.1002/rra.885>

1056 Sanchis-Ibor, C., Segura-Beltrán, F., Almonacid-Caballer, J., 2017. Channel forms recovery in an
1057 ephemeral river after gravel mining (Palancia River, Eastern Spain). *CATENA* 158, 357–370.
1058 <https://doi.org/10.1016/j.catena.2017.07.012>

1059 Sandmeier, K.J., 2016. ReflexW Version 8.1. Program for Processing of Seismic, Acoustic or
1060 Electromagnetic Reflection, Refraction and Transmission Data. Software Manual, Karlsruhe,
1061 Germany.

1062 Santaniello, D.J., Snyder, N.P., Gontz, A.M., 2013. Using ground-penetrating radar to determine the
1063 quantity of sediment stored behind the Merrimack Village Dam, Souhegan River, New Hampshire. In:
1064 De Graff, J.V., Evans, J.E., (Eds.), *The Challenges of Dam Removal and River Restoration:*
1065 *Geological Society of America Reviews in Engineering Geology*, v. XXI, pp. 45–57.
1066 [https://doi.org/10.1130/2013.4121\(04\)](https://doi.org/10.1130/2013.4121(04))

1067 Scorpio, V., Aucelli, P.P.C., Giano, S.I., Pisano, L., Robustelli, G., Roskopf, C.M., Schiattarella, M.,
1068 2015. River channel adjustments in Southern Italy over the past 150years and implications for channel
1069 recovery. *Geomorphology* 251, 77–90. <https://doi.org/10.1016/j.geomorph.2015.07.008>

1070 Scorpio, V., Roskopf, C.M., 2016. Channel adjustments in a Mediterranean river over the last 150
1071 years in the context of anthropic and natural controls. *Geomorphology* 275, 90–104.
1072 <https://doi.org/10.1016/j.geomorph.2016.09.017>

1073 Simon, A., Rinaldi, M., 2006. Disturbance, stream incision, and channel evolution: The roles of excess
1074 transport capacity and boundary materials in controlling channel response. *Geomorphology* 79, 361–
1075 383.

1076 Simon-Coinçon, R., Thiry, M., Quesnel, F., 2000. Paléopaysages et paléoenvironnements
1077 sidérolithiques du Nord du Massif central (France). *Comptes Rendus de l'Académie des Sciences -*
1078 *Series IIA - Earth and Planetary Science* 330, 693–700. <https://doi.org/10.1016/S1251->
1079 [8050\(00\)00189-0](https://doi.org/10.1016/S1251-8050(00)00189-0)

1080 Sreebha, S., Padmalal, D., 2011. Environmental impact assessment of sand mining from the small
1081 catchment rivers in the Southwestern coast of India: A case study. *Environ. Manag.* 47, 130–140.

1082 Stanford, J.A., Lorang, M.S., Hauer, F.R., 2005. The shifting habitat mosaic of river ecosystems.
1083 *Verh. Internat. Verein. Limnol.* 29 (1), 123–136. doi: 10.1080/03680770.2005.11901979

1084 Surian, N., Rinaldi, M., 2003. Morphological response to river engineering and management in
1085 alluvial channels in Italy. *Geomorphology* 50, 307–326.

1086 Surian, N., Rinaldi, M., Pellegrini, L., Audisio, C., Maraga, F., Teruggi, L., Turitto, O., Ziliani, L.,
1087 2009. Channel adjustments in northern and central Italy over the last 200 years. In James, L.A.,
1088 Rathburn, S.L., Whittecar, G.R.,(Eds)., *Management and Restoration of Fluvial Systems with Broad*
1089 *Historical Changes and Human Impacts: Geological Society of America Special Paper 451*, pp. 83–95.
1090 doi: 10.1130/2009.2451(05).

1091 Tabesh, M., Hoffmann, T., Vollmer, S., Schüttrumpf, H., Frings, R.M., 2019. In-situ measurement of
1092 river-bed sediment porosity using Structure-from-Motion image analysis. *Geomorphology* 338, 61–67.
1093 <https://doi.org/10.1016/j.geomorph.2019.04.011>

1094 Taylor, J., 1997. *An Introduction to Error Analysis: The Study of Uncertainties in Physical*
1095 *Measurements*. University Science Books, Sausalito, California.

1096 Tockner, K., Lorang, M.S., Stanford, J.A., 2010. River flood plains are model ecosystems to test
1097 general hydrogeomorphic and ecological concepts. *River. Res. Applic.* 26, 76–86.
1098 <https://doi.org/10.1002/rra.1328>

1099 Turland, M., Cojean, R., Brulhet, J., Morice, E., Grolier, J., Lacour, A., 1989a. *Carte géologique de*
1100 *France (1/50000), feuille de Hérisson (596)*. BRGM, Orléans.

1101 Turland, M., Hottin, A.M., Cojean, R., Ducreux, J.L., Debégliia, N., d'Arcy, D., Mathis, V., Carroué,
1102 J.P., Piboule, M., 1989b. *Notice explicative, carte géologique de France (1/50000), feuille de Hérisson*
1103 *(596)*. BRGM, Orléans (118 p).

1104 van Rijn, L.C., 1986. Sedimentation of Dredged Channels by Currents and Waves. *Journal of*
1105 *Waterway, Port, Coastal, and Ocean Engineering* 112, 541–559. [https://doi.org/10.1061/\(ASCE\)0733-](https://doi.org/10.1061/(ASCE)0733-)
1106 [950X\(1986\)112:5\(541\)](https://doi.org/10.1061/(ASCE)0733-950X(1986)112:5(541))

1107 Vayssière A., Dépret T., Castanet C., Gautier E., Virmoux C., Carcaud N., Garnier A., Brunstein D.,
1108 Pinheiro D., 2016. Etude des paléoméandres holocènes de la plaine alluviale du Cher (site de Bigny,
1109 moyenne vallée du Cher). *Géomorphologie : Relief, Processus, Environnement* 22 (2), 163–176.
1110 <https://doi.org/10.4000/geomorphologie.11369>

1111 Vayssière, A., Castanet, C., Gautier, E., Virmoux, C., Dépret, T., Gandouin, E., Develle-Vicent A.L.,
1112 Mokadem, F., Saulnier-Copard, S., Sabatier, P., Carcaud, N., 2020. Long-term readjustments of a
1113 sinuous river during the second half of the Holocene in northwestern Europe (Cher River, France).
1114 *Geomorphology* 370.

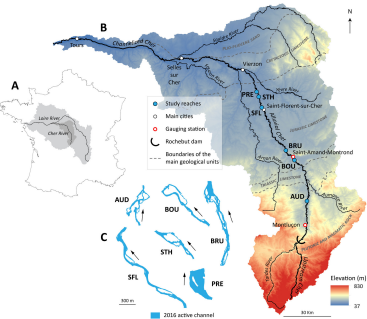
1115 Verstraeten, G., Poesen, J., 2001. Estimating trap efficiency of small reservoirs and ponds: methods
1116 and implications for the assessment of sediment yield. *Prog. Phys. Geogr.* 24 (2), 219–251.

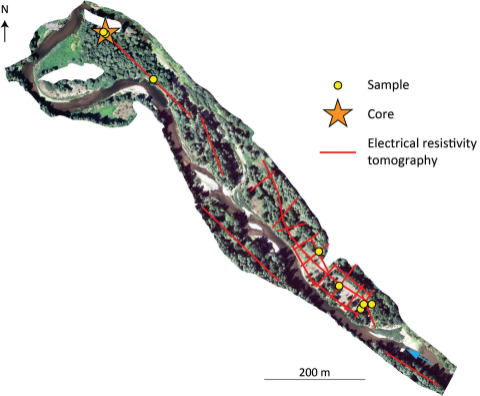
1117 Wilcock, P.R., Kenworthy, S.T., Crowe, J.C., 2001. Experimental study of the transport of mixed sand
1118 and gravel. *Water Resour. Res.* 37, 3349–3358. <https://doi.org/10.1029/2001WR000683>

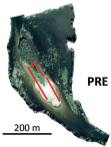
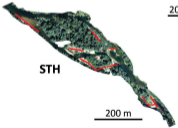
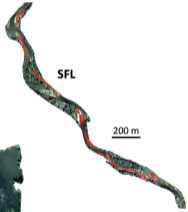
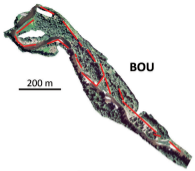
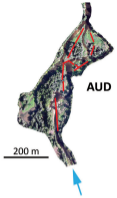
1119 Wyzga, B., 2007. A review on channel incision in the Polish Carpathian rivers during the 20th
1120 century. In: Habersack, H.M., Piégay, H., Rinaldi, M. (Eds.), *Gravel-bed rivers VI: From processes*
1121 *understanding to river restoration*. Elsevier, Amsterdam, pp. 525-555.

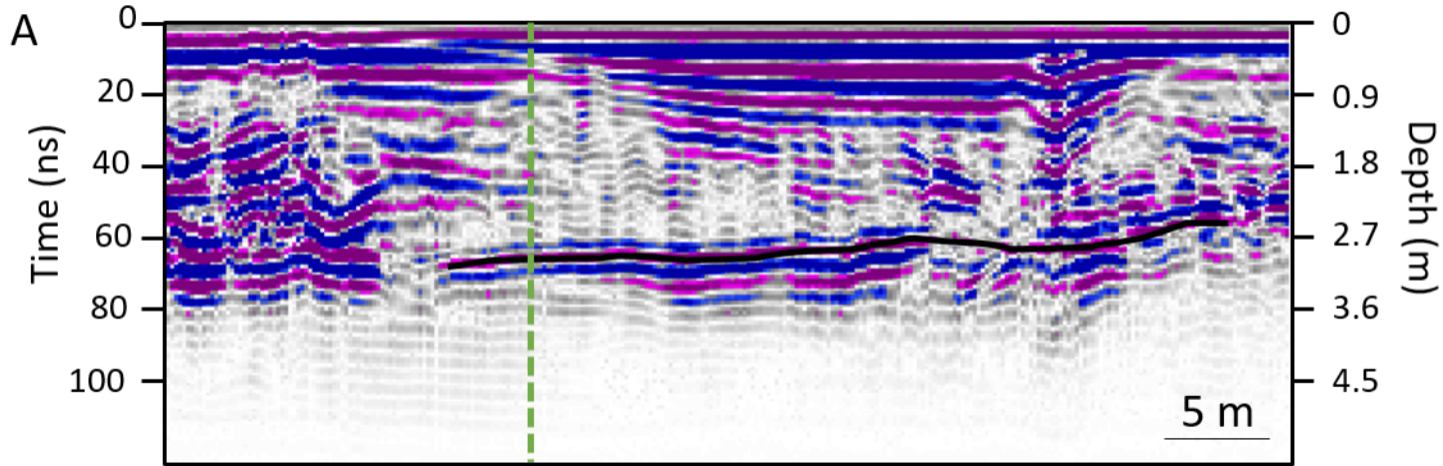
1122 Yuill, B.T., Gaweesh, A., Allison, M.A., Meselhe, E.A., 2016. Morphodynamic evolution of a lower
1123 Mississippi River channel bar after sand mining: In-channel Borrow Pit Infilling. *Earth Surf. Process.*
1124 *Landforms* 41, 526–542. <https://doi.org/10.1002/esp.3846>

1125 Ziegler, A.D., Sidle, R.C., Phang, V.X.H., Wood, S.H., Tantasirin, C., 2014. Bedload transport in SE
1126 Asian streams—Uncertainties and implications for reservoir management. *Geomorphology* 227, 31–
1127 48. <https://doi.org/10.1016/j.geomorph.2014.01.015>

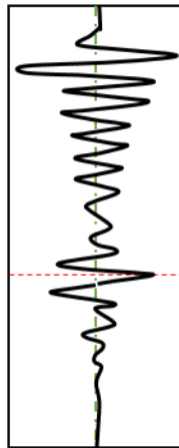


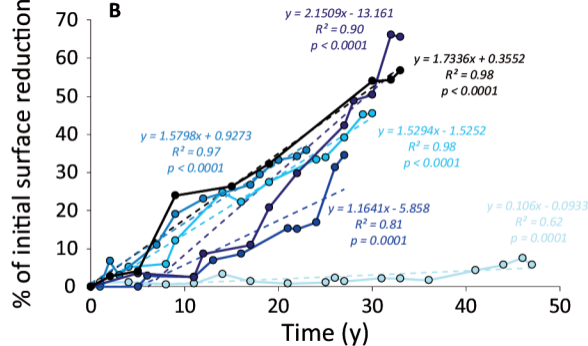
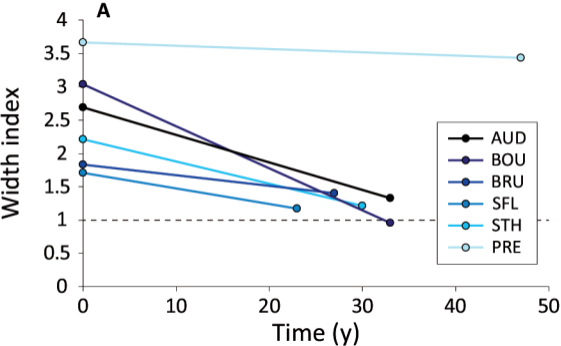


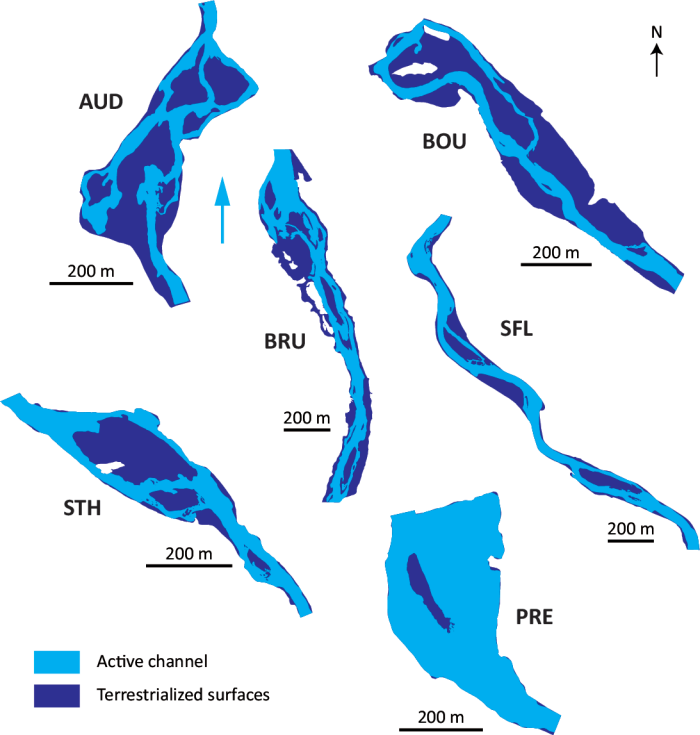


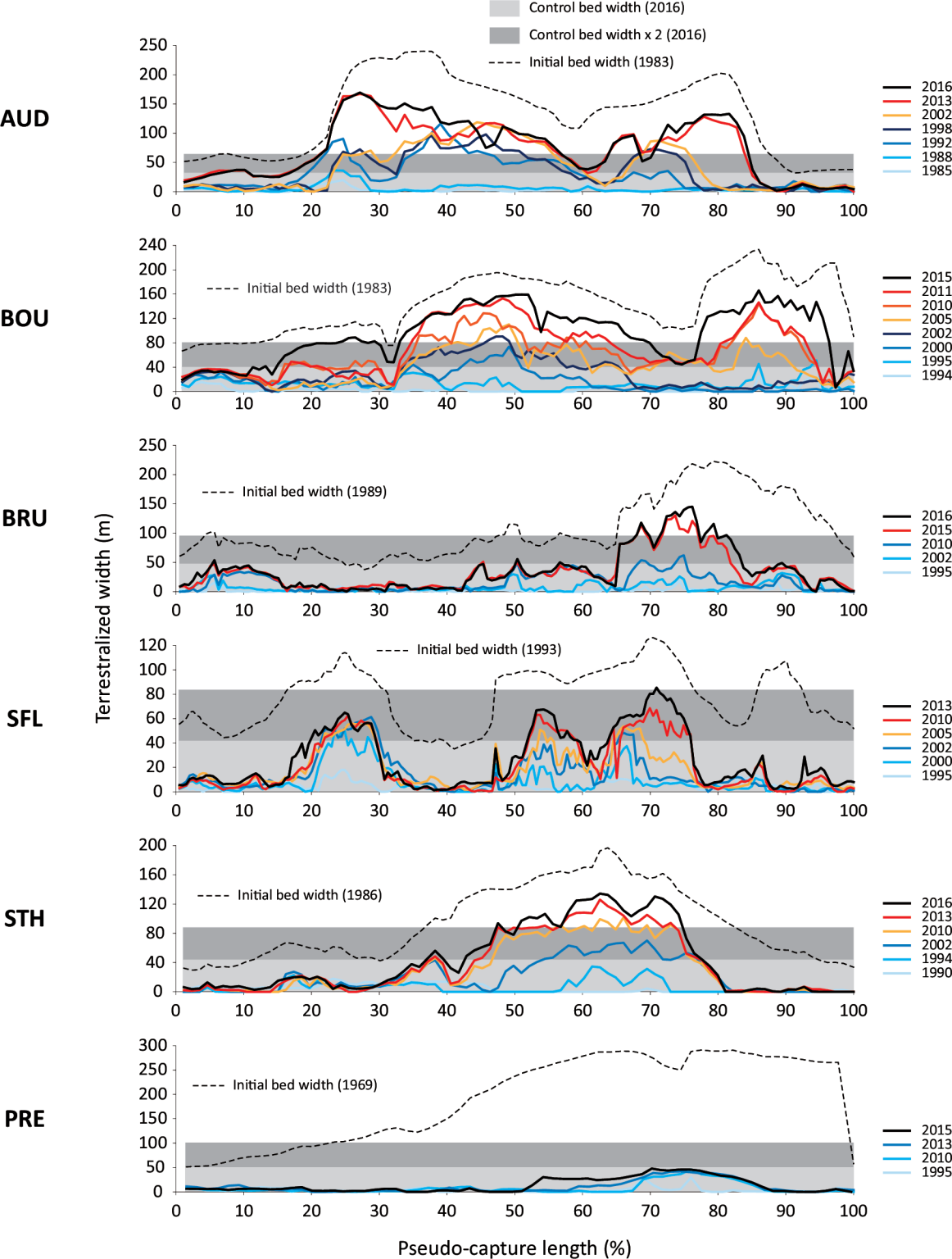


B

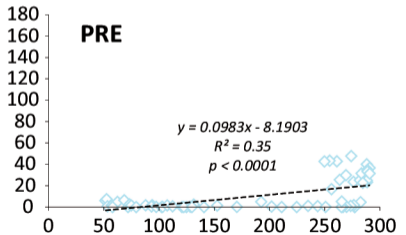
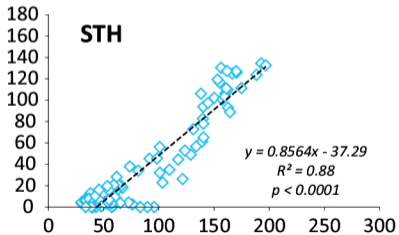
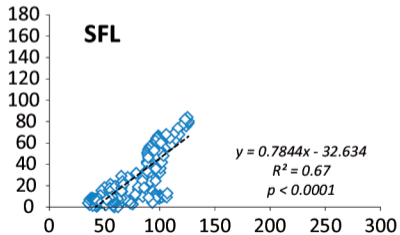
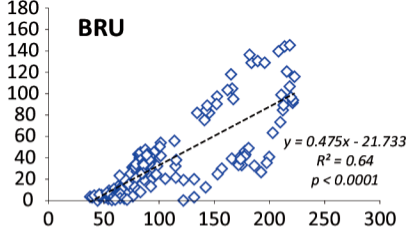
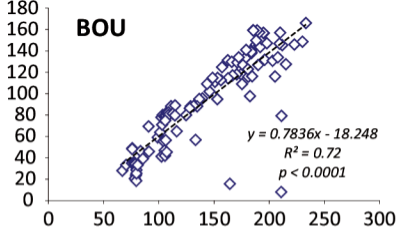
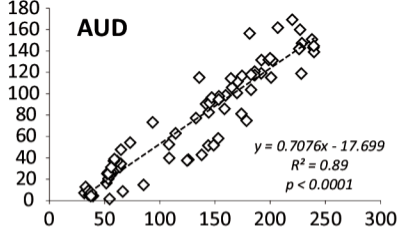




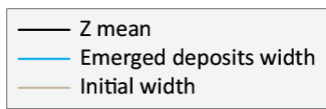
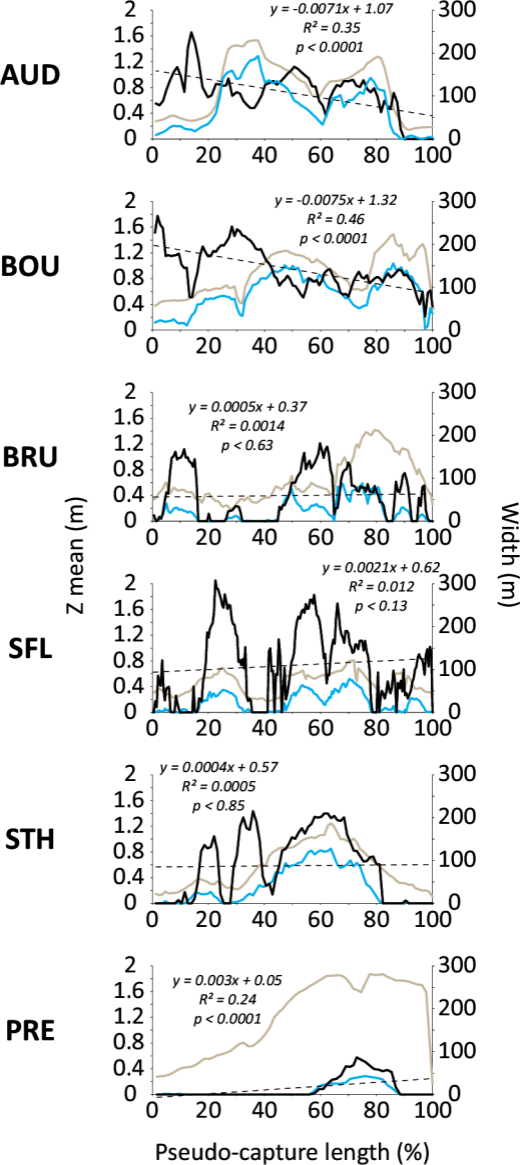


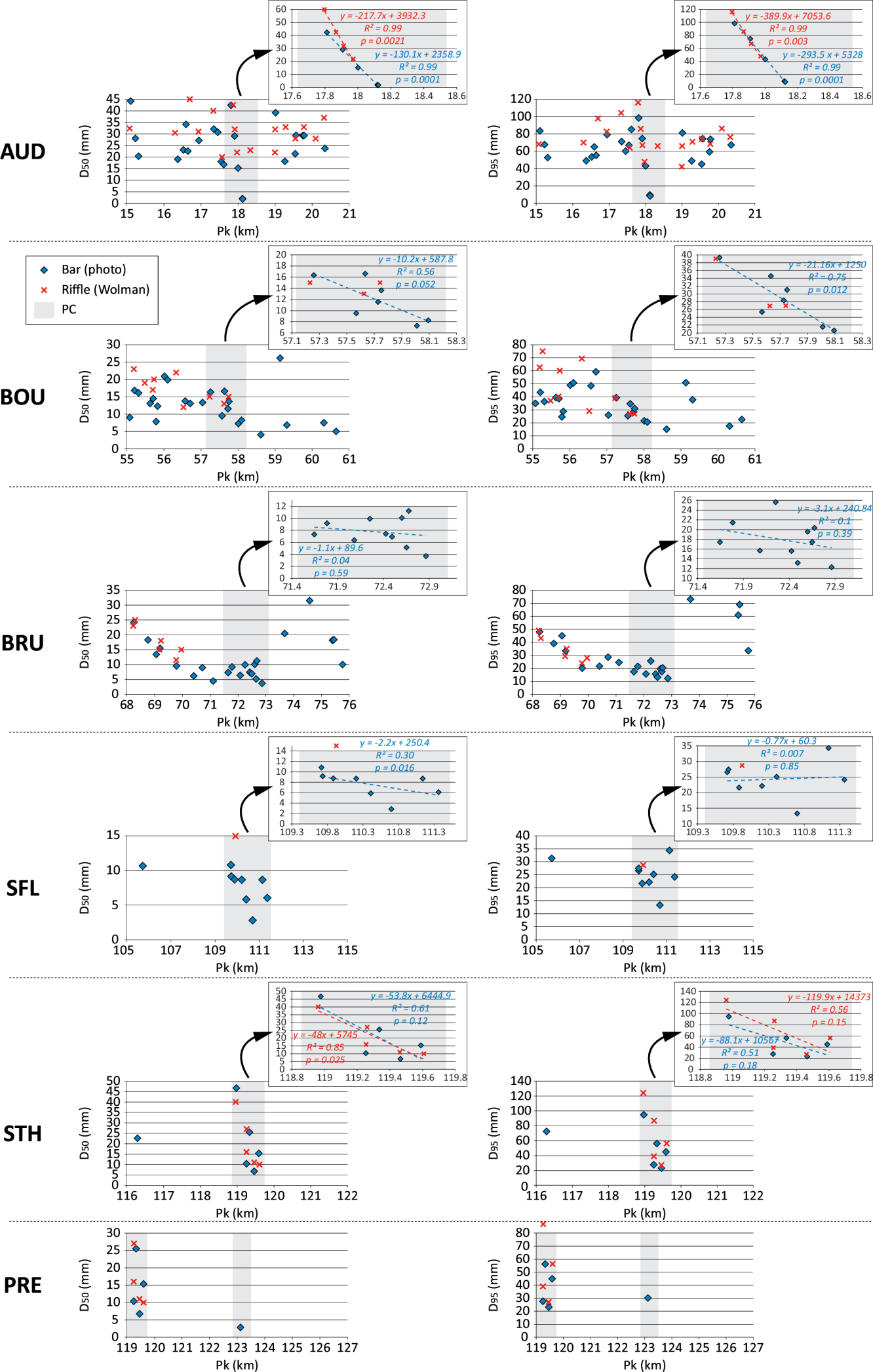


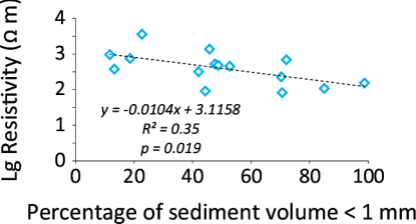
2016 terrestrial width (m)



Initial width (m)









- Sample
- Core
- Electrical resistivity tomography longitudinal profile
- Bedrock limit

